

1 **Is the recovery of stratospheric O₃ speeding up in the Southern Hemisphere?**

2 **An evaluation from the first IASI decadal record**

3
4 Catherine Wespes¹, Daniel Hurtmans¹, Simon Chabrillat², Gaétane Ronsmans¹, Cathy
5 Clerbaux^{3,1} and Pierre-François Coheur¹

6 ¹Université Libre de Bruxelles (ULB), Faculté des Sciences, Chimie Quantique et
7 Photophysique, Bruxelles, Belgique

8 ²Belgian Institute for Space Aeronomy, Brussels, Belgium

9 ³LATMOS/IPSL, Sorbonne Université, UVSQ, CNRS, Paris, France

10 11 **Abstract**

12 In this paper, we present the global fingerprint of recent changes in the mid-upper stratospheric
13 (MUS_t; <25hPa) ozone (O₃) in comparison with the lower stratospheric (LSt; 150-25 hPa) O₃
14 derived from the first 10 years of the IASI/Metop-A satellite measurements (January 2008 –
15 December 2017). The IASI instrument provides vertically-resolved O₃ profiles with very high
16 spatial and temporal (twice daily) samplings, allowing to monitor O₃ changes in these two
17 regions of the stratosphere. By applying multivariate regression models with adapted geophysical
18 proxies on daily mean O₃ time series, we discriminate anthropogenic trends from various modes
19 of natural variability, such as the El Niño/Southern Oscillation – ENSO. The representativeness
20 of the O₃ response to its natural drivers is first examined. One important finding relies on a
21 pronounced contrast between a positive LSt O₃ response to ENSO in the extra-tropics and a
22 negative one in the tropics, with a delay of 3 months, which supports a stratospheric pathway for
23 the ENSO influence on lower stratospheric and tropospheric O₃. In terms of trends, we find an
24 unequivocal O₃ recovery from the available period of measurements in winter/spring at mid-high
25 latitudes for the two stratospheric layers sounded by IASI (>~35°N/S in the MUS_t and >~45°S in
26 the LSt) as well as in the total columns at southern latitudes (>~45°S) where the increase reaches
27 its maximum. These results confirm the effectiveness of the Montreal protocol and its
28 amendments, and represent the first detection of a significant recovery of O₃ concurrently in the
29 lower, in the mid-upper stratosphere and in the total column from one single satellite dataset. A
30 significant decline in O₃ at northern mid-latitudes in the LSt is also detected, especially in
31 winter/spring of the northern hemisphere. Given counteracting trends in LSt and MUS_t at these
32 latitudes, the decline is not categorical in total O₃. When freezing the regression coefficients
33 determined for each natural driver over the whole IASI period but adjusting a trend, we calculate
34 a significant speeding up in the O₃ response to the decline of O₃ depleting substances (ODS) in
35 the total column, in the LSt and, to a lesser extent, in the MUS_t, at high southern latitudes over
36 the year. Results also show a small significant acceleration of the O₃ decline at northern mid-
37 latitudes in the LSt and in the total column over the last years. That, specifically, needs urgent
38 investigation for identifying its exact origin and apprehending its impact on climate change.

39 Additional years of IASI measurements would, however, be required to confirm the O₃ change
40 rates observed in the stratospheric layers over the last years.

41

42 **1 Introduction**

43

44 Ozone is a key radiatively active gas of the Earth atmosphere, in both the troposphere and the
45 stratosphere. While, in the troposphere, O₃ acts as a strong pollutant and an important
46 greenhouse gas, in the stratosphere and, more particularly, in the middle-low stratosphere, it
47 forms a protective layer for life on Earth against harmful solar radiation. In the 1980s, the
48 scientific community motivated decision-makers to regulate the use of chlorofluorocarbons
49 (CFCs), after the unexpected discovery of the springtime Antarctic ozone hole (Chubachi, 1984;
50 Farman et al., 1985) that was suspected to be induced by continued use of CFCs (Molina and
51 Rowland, 1974; Crutzen, 1974); The O₃ depletion was later verified from measurements at other
52 Antarctic sites (e.g. Farmer et al., 1987) and from satellite observations (Stolarski et al., 1986),
53 and explained by the role of CFC's on the massive destruction of O₃ following heterogeneous
54 reactions on the surface of polar stratospheric clouds (Solomon, 1986; 1999 and references
55 therein). The world's nations reacted to that human-caused worldwide problem by ratifying the
56 International Vienna Convention for the Protection of the Ozone Layer in 1985 and the Montreal
57 Protocol in 1987 with its later amendments, which forced the progressive banning of these ozone
58 depleting substances (ODS) in industrial applications by early 1990s with a total phase-out of the
59 most harmful CFCs by the year 2000.

60

61 A recovery from O₃ depletion is expected in response to the Montreal Protocol and its
62 amendments, but with a delayed period due to the long residence time of halocarbons in the
63 atmosphere (Hofmann et al., 1997; Dhomse et al., 2006; WMO, 2007; 2011). The decline of
64 CFCs in the stratosphere was only initiated about 10 years after their phasing out (Anderson et
65 al., 2000; Newman et al., 2006; Solomon et al., 2006; Mäder et al., 2010; WMO, 2011; 2014).
66 The early signs of ozone response to that decline were identified in several studies that reported
67 first a slowdown in stratospheric ozone depletion (e.g. Newchurch et al., 2003; Yang et al.,
68 2008), followed by a leveling off of upper stratospheric (e.g. WMO, 2007) and total O₃ (e.g.
69 WMO, 2011; Shepherd et al., 2014) depletion since the 2000's. A significant onset of recovery
70 was identified later for upper stratospheric O₃ (e.g. WMO, 2014; 2018; Harris et al., 2015). Only
71 a few studies have shown evidence for increasing total column O₃ in polar regions during
72 springtime (e.g. Salby et al., 2011; Kuttippurath et al., 2013; Shepherd et al., 2014; Solomon et
73 al., 2016). Statistically significant long-term recovery in total O₃ column (TOC) on a global scale
74 has not yet been observed, likely because of counteracting trends in the different vertical
75 atmospheric layers. Ball et al. (2018) have found that a continuing O₃ decline prevails in the
76 lower stratosphere since 1998, leading to a slower increase in total O₃ than expected from the
77 effective equivalent stratospheric chlorine (EESC) decrease. However, the reported decline is not
78 reproduced by the state-of-the-art models and its exact reasons are still unknown (Ball et al.,

79 2018). Wargan et al. (2018) and Galytska et al. (2019) recently reported that the decline in the
80 extratropical lower stratosphere and tropical mid-stratosphere is dynamically controlled by
81 variations in the tropical upwelling.

82
83 Although recent papers based on observational datasets and statistical approaches agree that we
84 currently progress towards an emergence into ozone recovery (e.g. Pawson et al., 2014; Harris et
85 al., 2015; Steinbrecht et al., 2017; Sofieva et al., 2017; Ball et al., 2018; Weber et al., 2018),
86 trend magnitude and trend significance over the whole stratosphere substantially differ from one
87 study to another and, consequently, they are still subject to uncertainty (Keeble et al., 2018). A
88 clear identification of the onset of O₃ recovery is very difficult due to concurrent sources of O₃
89 fluctuations (e.g. Reinsel et al., 2005; WMO, 2007, 2011). They include: changes in solar
90 ultraviolet irradiance, in atmospheric circulation patterns such as the quasi-biennial oscillation
91 (QBO; Baldwin et al., 2001) and the El Niño–Southern Oscillation (ENSO; e.g. Randel et al.,
92 2009), in temperature, in ODS emissions and volcanic eruptions (e.g. Mt Pinatubo in 1991 and
93 Calbuco in 2015) with their feedbacks on stratospheric temperature and dynamics (e.g. Jonsson
94 et al., 2004). Furthermore, the differences in vertical/spatial resolution and in retrieval
95 methodologies (inducing biases), possible instrumental degradations (inducing drifts), and use of
96 merged datasets into composites, likely explain part of the trend divergence between various
97 studies. Merging may be performed on deseasonalized anomalies, which offers the advantage of
98 removing instrumental biases between the individual data records (Sofieva et al., 2017) but large
99 differences remain in anomaly values between the independent datasets, as well as large
100 instrumental drifts and drift uncertainty estimates that prevent deriving statistically accurate
101 trends (Harris et al., 2015; Hubert et al., 2016).

102
103 In this context, there is a pressing need for long-duration, high-density and homogenized O₃
104 profile dataset to assess significant O₃ changes in different parts of the stratosphere and their
105 contributions to the total O₃.

106
107 In this paper, we exploit the high frequency (daily) and spatial coverage of the IASI satellite
108 dataset over the first decade of the mission (January 2008 – December 2017) to determine global
109 patterns of reliable trends in the stratospheric O₃ records, separately in the Mid-Upper
110 Stratosphere (MUS_t) and the Lower Stratosphere (LS_t). This study is built on previous analysis
111 of stratospheric O₃ trends from IASI, estimated on latitudinal averages over a shorter period
112 (2008-2013) (Wespes et al., 2016). A multivariate linear regression (MLR) model (annual and
113 seasonal formulations) that is similar to that previously used for tropospheric O₃ studies from
114 IASI (Wespes et al., 2017; 2018), but adapted here for the stratosphere with appropriate drivers,
115 is applied to gridded daily mean O₃ time series in the MUS_t and the LS_t. The MLR model is
116 evaluated in terms of its performance and its ability to capture the observed variability in Section
117 2, in terms of representativeness of O₃ drivers in Section 3 and in terms of adjusted trends in
118 Section 4. The minimum numbers of years of IASI measurements that is required to indeed

119 detect the adjusted trends from MLR in the two layers is also estimated in Section 4 that ends
120 with an evaluation of the trends detectable in polar winter and spring and with an evaluation of a
121 speeding up in the O₃ changes.

122

123 **2 Dataset and methodology**

124

125 **2.1 IASI O₃ data**

126

127 The Infrared Atmospheric Sounding Interferometer (IASI) is a nadir-viewing Fourier transform
128 spectrometer designed to measure the thermal infrared emission of the Earth-atmosphere system
129 between 645 and 2760 cm⁻¹. Measurements are taken from the polar sun-synchronous orbiting
130 meteorological Metop series of satellites, every 50 km along the track of the satellite at nadir and
131 over a swath of 2200 km across track. With more than 14 orbits a day and a field of view of four
132 simultaneous footprints of 12 km at nadir, IASI provides global coverage of the Earth twice a
133 day at about 09:30 AM and PM mean local solar time.

134

135 The Metop program consists of a series of three identical satellites successively launched to
136 ensure homogenous measurements covering more than 15 years. Metop-A and -B have been
137 successively launched in October 2006 and September 2012. The third and last satellite was
138 launched in November 2018 onboard Metop-C. In addition to its exceptional spatio-temporal
139 coverage, IASI also provides good spectral resolution and low radiometric noise, which allows
140 the measurement of a series of gas-phase species and aerosols globally (e.g. Clerbaux et al.,
141 2009; Hilton et al., 2012; Clarisse et al., 2018).

142

143 For this study, we use the O₃ profiles retrieved by the Fast Optimal Retrievals on Layers for IASI
144 (FORLI-O₃; version 20151001) near-real time processing chain set up at ULB (See Hurtmans et
145 al, 2012 for a description of the retrieval parameters and the FORLI performances). The FORLI
146 algorithm relies on a fast radiative transfer and a retrieval methodology based on the Optimal
147 Estimation Method (Rodgers, 2000) that requires a priori information (a priori profile and
148 associated variance-covariance matrix). The FORLI-O₃ a priori consists of one single profile and
149 one covariance matrix built from the global Logan/Labow/McPeters climatology (McPeters et
150 al., 2007). The profiles are retrieved on a uniform 1 km vertical grid on 41 layers from surface to
151 40 km with an extra layer from 40 km to the top of the atmosphere considered at 60 km. Previous
152 characterization of the FORLI-O₃ profiles (Wespes et al., 2016) have demonstrated a good
153 vertical sensitivity of IASI to the O₃ measurement with up to 4 independent levels of information
154 on the vertical profile in the troposphere and the stratosphere (MUS_t; LSt; upper troposphere-
155 lower stratosphere – UTLS – 300-150 hPa; middle-low troposphere – MLT – below 300 hPa).
156 The two stratospheric layers that show distinctive patterns of O₃ distributions over the IASI
157 decade (Fig. 1a) are characterized by high sensitivity (DOFS > 0.85; Fig. 1b) and low total
158 retrieval errors (<5%; see Hurtmans et al., 2012; Wespes et al., 2016). The decorrelation between

159 the MUST and the LSt is further evidenced in Fig. 1d that shows low correlation coefficients (<
160 0.4) between the mean absolute deseasonalized anomalies (as calculated in Wespes et al., 2017)
161 in the two layers (Fig. 1c). Note that the highest correlation coefficients over the Antarctic (~0.4)
162 are due to the smaller vertical sensitivity of the IASI measurements over cold surface (Clerbaux
163 et al., 2009). The latest validation exercises for the FORLI-O₃ product have demonstrated a high
164 degree of precision with excellent consistency between the measurements taken from the two
165 IASI instruments on Metop-A and -B, as well as a good degree of accuracy with biases lower
166 than 20% in the stratospheric layers (Boynard et al., 2018; Keppens et al. 2017). Thanks to these
167 good IASI-FORLI performances, large-scale dynamical modes of O₃ variations and long-term O₃
168 changes can be differentiated in the four retrieved layers (Wespes et al., 2016). The recent
169 validations have, however, reported a drift in the MUST FORLI-O₃ time series from comparison
170 with O₃ sondes in the northern hemisphere (N.H.) ($\sim 3.53 \pm 3.09$ DU.decade⁻¹ on average over
171 2008–2016; Boynard et al., 2018) that was suggested to result from a pronounced discontinuity
172 (“jump”) rather than from a progressive change. Further comparisons with CTM simulations
173 from the Belgian Assimilation System for Chemical Observations (BASCOE; Chabrillat et al.,
174 2018; Errera et al., 2019) confirm this jump that occurred on 15 September 2010 over all
175 latitudes (see Fig. S1 of the supplementary materials). The discontinuity is suspected to result
176 from updates in level-2 temperature data from Eumetsat that are used as inputs into FORLI (see
177 Hurtmans et al., 2012). Hence, the apparent drift reported by Boynard et al. (2018) likely results
178 from the jump rather than from a progressive “instrumental” drift. This is verified by the absence
179 of drift in the O₃ time series after the jump (non-significant drift of -0.38 ± 2.24 DU.decade⁻¹ on
180 average over October 2010 – May 2017; adapted from Boynard et al., 2018). This is in line with
181 the excellent stability of the IASI Level-1 radiances over the full IASI period (Buffet et al.,
182 2016). From the IASI-BASCOE comparisons, the amplitude of the jump has been estimated as
183 lower than 2.0 DU in the 55°S–55°N latitude band and 4.0 DU in the 55°–90° latitude band of
184 each hemisphere. The estimated amplitude of the jump is found to be relatively small in
185 comparison to that of the decadal trends derived in Section 4, hence, it cannot explain the
186 tendency in the IASI dataset. Therefore, the jump is not taken into account in the MLR. The
187 jump values will be, however, considered in the discussion of the O₃ trends (Section 4).

188

189 Finally, the present study only uses the daytime measurements (defined with a solar zenith angle
190 to the sun < 83°) from the IASI-A (aboard Metop-A) instrument that fully covers the first decade
191 of the IASI mission. The daytime measurements are characterized by a higher vertical sensitivity
192 (e.g. Clerbaux et al., 2009). Quality flags developed in previous IASI studies (e.g. Boynard et al.,
193 2018) were applied a posteriori to exclude data with a poor spectral fit, with less reliability or
194 with cloud contamination.

195

196 **2.2 Multivariate regression model**

197

198 In an effort to unambiguously discriminate anthropogenic trends in O₃ levels from the various
 199 modes of natural variability (illustrated globally in Fig.1c as deseasonalized anomalies), we have
 200 applied to the 2.5°x2.5° gridded daily MUST and LSt O₃ time series, a MLR model that is similar
 201 to that previously developed for tropospheric O₃ studies from IASI (see Wespes et al., 2017;
 202 2018) but here adapted to fit the stratospheric variations:
 203

$$204 \quad O_3(t) = Cst + x_{j=1} \cdot trend + \sum_{n=1:2} [a_n \cdot \cos(n\omega t) + b_n \cdot \sin(n\omega t)] + \sum_{j=2}^m x_j X_{norm,j}(t) + \varepsilon(t) \quad (1)$$

205
 206 where t is the number of days, x_1 is the trend coefficient in the data, $\omega = 2\pi/365.25$, a_n, b_n, x_j are
 207 the regression coefficients of the seasonal and non-seasonal variables and $\varepsilon(t)$ is the residual
 208 variation (assumed to be autoregressive with time lag of 1 day). $X_{norm,j}$ are the m chosen
 209 explanatory variables, commonly called “proxies”, which are normalized over the study period
 210 (2008 – 2017) with:

$$211 \quad X_{norm}(t) = 2[X(t) - X_{median}] / [X_{max} - X_{min}] \quad (2)$$

212
 213 In addition to harmonic terms that represent the 1-yr and 6-month variations, the MLR model
 214 includes the anthropogenic O₃ response through a linear trend (LT) term and a set of proxies to
 215 parameterize the geophysical processes influencing the abundance of O₃ in the stratosphere. The
 216 MLR uses an iterative stepwise backward elimination approach to retain, at the end of the
 217 iterations, the most relevant proxies (with a 95% confidence level) explaining the O₃ variations
 218 (e.g. Mäder et al., 2007). Table 1 lists the selected proxies, their sources and their temporal
 219 resolutions. The proxies describe the influence of the Quasi-Biennial Oscillation (QBO; visible
 220 from the deseasonalized anomaly maps in Fig.1c with a typical band-like pattern around the
 221 Equator) at 10 hPa and 30 hPa, of the North Atlantic and the Antarctic Oscillations (NAO and
 222 AAO), of the El Niño/Southern Oscillation (ENSO), of the volcanic aerosols (AERO) injected
 223 into the stratosphere, of the strength of the Brewer-Dobson circulation (BDC) with the Eliassen-
 224 Palm flux (EPF), of the polar O₃ loss driven by the volume of polar stratospheric clouds (VPSC),
 225 of the tropopause height variation with the geopotential height (GEO) and of the mixing of
 226 tropospheric and stratospheric air masses with the potential vorticity (PV). The main proxies in
 227 terms of their influence on O₃ are illustrated in Fig. 2 over the period of the IASI mission. The
 228 construction of the EPF, VPSC and AERO proxies, which are specifically used in this study, is
 229 explained hereafter, while the description of the other proxies can be found in previous IASI
 230 studies (Wespes et al., 2016; 2017).
 231

232
 233 The EPF proxy consists of the normalized upward component of the EP flux crossing 100 hPa
 234 and spatially averaged over the 45°-75° latitude band for each hemisphere. The fluxes are

235 calculated from the NCEP/NCAR 2.5°x2.5° gridded daily reanalysis (Kalnay et al., 1996) over
236 the IASI decade. The VPSC proxy is based on the potential volume of PSCs given by the volume
237 of air below the formation temperature of nitric acid trihydrate (NAT) over 60°-90° north and
238 south and calculated from the ERA-Interim reanalysis and from the MLS climatology of nitric
239 acid (I. Wohltmann, private communication; Wohltmann et al., 2007; and references therein).
240 The PSC volume is multiplied by the EESC to account for the changes in the amount of
241 inorganic stratospheric chlorine that activates the polar ozone loss. The O₃ build-up and the polar
242 O₃ loss are highly correlated with wintertime accumulated EP flux and PSC volume, respectively
243 (Fusco and Salby, 1999; Randel et al., 2002; Fioletov and Shepherd, 2003 and Rex et al., 2004).
244 These cumulative EP flux and PSC effects on O₃ levels are taken into account by integrating the
245 EPF and VPSC proxies over time with a specific exponential decay time according to the
246 formalism of Brunner et al. (2006; see Eq. 4). We set the relaxation time scale to 3 months
247 everywhere, except during the wintertime build-up phase of O₃ in the extratropics (from October
248 to March in the N.H. and from April to September in the southern hemisphere - S.H.) when it is
249 set to 12 months. For EPF, it accounts for the slower relaxation time of extratropical O₃ in winter
250 due to its longer photochemical lifetime. For VPSC, the 12-month relaxation time accounts for a
251 stronger effect of stratospheric chlorine on spring O₃ levels: the maximum of the accumulated
252 VPSC (Fig. 2) coincides with the maximum extent of O₃ hole that develops during springtime
253 and that lasts until November. Note that correlations between VPSC and EPF are possible since
254 the same method is used to build these cumulative proxies. VPSC and EPF are also dynamically
255 anti-correlated to some extent since a strong BDC is connected with warm polar stratospheric
256 temperatures and, hence, reduced PSC volume (e.g. Wohltmann et al., 2007).

257
258 The AERO proxy is derived from aerosol optical depth (AOD) of sulfuric acid only. That proxy
259 consists of latitudinally averaged (22.5°N-90°N – AERO-N, 22.5°S-90°S – AERO-S and 22.5°S-
260 22.5°N – AERO-Eq) extinction coefficients at 12 μm calculated from merged aerosol datasets
261 (SAGE, SAM, CALIPSO, OSIRIS, 2D-model-simulation and Photometer; Thomason et al.,
262 2018) and vertically integrated over the two IASI stratospheric O₃ columns (AERO-MUSt and
263 AERO-LSt). Fig.2 shows the AERO proxies (AERO-N, AERO-S and AERO-Eq) corresponding
264 to the AOD over the whole stratosphere (150-2 hPa), while Fig.3 represents the latitudinal
265 distribution of the volcanic sulfuric acid extinction coefficients integrated over the whole
266 stratosphere (top panel) and, separately, over the MUSt (middle panel) and the LSt (bottom
267 panel) from 2005 to 2017. The AOD distributions indicate the need for considering one specific
268 AERO proxy for each latitudinal band (AERO-N, AERO-S and AERO-Eq) and for each vertical
269 layer (AERO-MUSt and AERO-LSt). Note that, as an alternative proxy to AERO, the surface
270 area density of ambient aerosol, that represents the aerosol surface available for chemical
271 reactions, has been tested, giving similar results.

272
273 Note also that, similarly to what has already been found for tropospheric O₃ from IASI (Wespes
274 et al., 2016), several time-lags for ENSO (1-, 3- and 5-month lags; namely, ENSO-lag1, ENSO-

275 lag3 and ENSO-lag5) are also included in the MLR model to account for a possible delay in the
276 O₃ response to ENSO at high latitudes.

277

278 Finally, autocorrelation in the noise residual $\varepsilon(t)$ (see Eq. 1 in Wespes et al., 2016) is accounted
279 for in the MLR analysis with time lag of one day to yield the correct estimated standard errors
280 for the regression coefficients. They are estimated from the covariance matrix of the regression
281 coefficients and corrected at the end of the iterative process by the autocorrelation of the noise
282 residual. The regression coefficients are considered significant if they fall in the 95% confidence
283 level (defined by 2σ level).

284

285 In the seasonal formulation of the MLR model, the main proxies ($x_j X_{norm,j}$; with x_j , the
286 regression coefficient and $X_{norm,j}$, the normalized proxy) are split into four seasonal functions
287 ($x_{spr} X_{norm,spr} + x_{sum} X_{norm,sum} + x_{fall} X_{norm,fall} + x_{wint} X_{norm,wint}$) that are independently and
288 simultaneously adjusted for each grid cell (Wespes et al., 2017). Hence, the seasonal MLR
289 adjusts 4 coefficients (instead of one in the annual MLR) to account for the seasonal O₃ response
290 to changes in the proxy. If that method avoids to over-constrain the adjustment by the year-round
291 proxies and, hence, reduces the systematic errors, the smaller daily data points covered by the
292 seasonal proxies translate to a lower significance of these proxies. This is particularly true for
293 EPF and VPSC that compensate each other by construction. As a consequence, the annual MLR
294 is performed first in this study and, then, complemented with the seasonal one when it is found
295 helpful for further interpreting the observations.

296

297 Figure 4 shows the latitudinal distributions of the O₃ columns in the two stratospheric layers over
298 the IASI decade (first panels in Fig.4 a and b), as well as those simulated by the annual MLR
299 regression model (second panels) along with the regression residuals (third panels). The root
300 mean square error (*RMSE*) of the regression residual and the contribution of the MLR model into

301 the IASI O₃ variations (calculated as $\frac{\sigma(O_3^{\text{Fitted_model}}(t))}{\sigma(O_3(t))}$ where σ is the standard deviation relative

302 to the regression model and to the IASI time series; bottom panels) are also represented (bottom
303 panels). The results indicate that the model reproduces ~25-85% and ~35-95% of the daily O₃
304 variations captured by IASI in the MUST and the LSt, respectively, and that the residual errors
305 are generally lower than 10% everywhere for the two layers, except for the spring O₃ hole region
306 in the LSt. The *RMSE* relative to the IASI O₃ time series are lower than 15 DU and 20 DU at
307 global scale in the MUST and the LSt, respectively, except around the S.H. polar vortex in the
308 LSt (~30 DU). On a seasonal basis (figure not shown), the results are only slightly improved: the
309 model explains from ~35-90% and ~45-95% of the annual variations and the *RMSE* are lower
310 than ~12 DU and ~23 DU everywhere, in the MUST and the LSt, respectively. These results
311 verify that the MLR models (annual and seasonal) reproduce well the time evolution of O₃ over

312 the IASI decade in the two stratospheric layers and, hence, that they can be used to identify and
313 quantify the main O₃ drivers in these two layers (see Section 3).

314

315 The MLR model has also been tested on nighttime FORLI-O₃ measurements only and
316 simultaneously with daytime measurements, but this resulted in a lower quality fit, especially in
317 the MUST over the polar regions. This is due to the smaller vertical sensitivity of IASI during
318 nighttime measurements, especially over cold surface, which causes larger correlations between
319 stratospheric and tropospheric layers (e.g. 40-60% at high northern latitudes versus ~10-20% for
320 daytime measurements based on deseasonalized anomalies) and, hence, which mixes
321 counteracting processes from these two layers. For this reason, only the results for the MLR
322 performed on daytime measurements are presented and discussed in this paper.

323

324 **3 Drivers of O₃ natural variations**

325

326 Ascribing a recovery in stratospheric O₃ to a decline in stratospheric halogen species requires
327 first identifying and quantifying natural cycles that may produce trend-like segments in the O₃
328 time series, in order to prevent any misinterpretation of those segments as signs of O₃ recovery.
329 The MLR analysis performed in Section 2.2 that was found to give a good representation of the
330 MUST and LSt O₃ records shows distinctive relevant patterns for the individual proxies retained
331 in the regression procedure, as represented in Fig. 5. The fitted drivers are characterized by
332 significant regional differences in their regression coefficients with regions of in-phase relation
333 (positive coefficients) or out-of-phase relation (negative coefficients) with respect to the IASI
334 stratospheric O₃ anomalies. The areas of significant drivers (in the 95% confidence limit) are
335 surrounded by non-significant cells when accounting for the autocorrelation in the noise residual.
336 Figures 6 a and b respectively represent the latitudinal averages of the fitted regression
337 coefficients for the significant proxies showing latitudinal variation only in the O₃ response
338 (namely, QBO, EPF, VPSC, AERO and ENSO) and of the contribution of these drivers into the
339 O₃ variability (calculated as the product of the 2 σ variability of each proxy by its corresponding
340 fitted coefficient, i.e. the 2 σ variability of the reconstructed proxies). The 2 σ O₃ variability in the
341 IASI measurements and in the fitted MLR model are also represented (black and grey lines,
342 respectively). Figure 7 displays the same results as Fig. 6b but for the austral spring and winter
343 periods only (using the seasonal MLR).

344

345 The PV and GEO proxies are generally minor components (not shown here) with relative
346 contributions smaller than 10% and large standard errors (>80%), except in the tropics where the
347 contribution for GEO reaches 40% in the LSt due to the tropopause height variation. Each other
348 adjusted proxy (QBO, SF, EPF, VPSC, AERO, ENSO, NAO and AAO) is an important
349 contributor to the O₃ variations, depending on the layer, region, and season as described next:

350

- 351 1. QBO - The QBO at 10hPa and 30hPa are important contributors around the Equator for
352 the two stratospheric layers. It shows up as a typical band-like pattern of high positive
353 coefficients confined equatorward of $\sim 15^\circ\text{N/S}$ where the QBO is known to be a dominant
354 dynamical modulation force associated with strong convective anomalies (e.g. Randel
355 and Wu, 1996; Tian et al., 2006; Witte et al., 2008). In that latitude band, QBO10 and
356 QBO30 explain up to ~ 8 DU and ~ 5 DU, respectively, of the MUST and LSt yearly O_3
357 variations (see Fig. 5 and 6b; i.e. relative contributions up to $\sim 50\%$ and $\sim 40\%$ for
358 QBO10/30 in MUST and LSt O_3 , respectively). The QBO is also influencing O_3 variations
359 poleward of 60°N/S with a weaker correlation between O_3 and equatorial wind anomalies
360 as well as in the sub-tropics with an out-of-phase transition. That pole-to-pole QBO
361 influence results from the QBO-modulation of extra-tropical waves and its interaction
362 with the BDC (e.g. Fusco and Salby, 1999). A pronounced seasonal dependence is
363 observed in the out-of-phase sub-tropical O_3 anomalies in the MUST, with the highest
364 amplitude oscillating between the hemispheres in their respective winter (~ 5 DU of O_3
365 variations explained by QBO10/30 at $\sim 20^\circ\text{S}$ during JJA and at $\sim 20^\circ\text{N}$ during DJF; see
366 Fig. 7b for the JJA period in the MUST the DJF period is not shown), which is in
367 agreement with Randel and Wu (1996). The amplitude of the QBO signal is found to be
368 stronger for QBO30 than for QBO10 in the LSt, which is in good agreement with studies
369 from other instruments for the total O_3 (e.g. Baldwin et al., 2001; Steinbrecht et al., 2006;
370 Frossard et al., 2013; Coldewey-Egbers et al., 2014) and from IASI in the troposphere
371 (Wespes et al., 2017). The smaller amplitude of O_3 response to QBO10 in the LSt
372 compared to the MUST is again in agreement with previous studies that reported changes
373 in phase of the QBO10 response as a function of altitude with a positive response in the
374 upper stratosphere and destructive interference in the mid-low stratosphere (Chipperfield
375 et al., 1994; Brunner et al., 2006).
- 376
- 377 2. SF - In the MUST layer, the solar cycle O_3 response is one of the strongest contributors
378 and explains globally between ~ 2 and 15 DU of in-phase O_3 variations (i.e. higher O_3
379 values during maximum solar irradiance) with the largest amplitude over the highest
380 latitude regions (see Fig. 5; relative contribution up to $\sim 20\%$). The solar influence in LSt
381 is more complex with regions of in-phase and out-of-phase O_3 variations. The impact of
382 solar variability on stratospheric O_3 abundance is due to a combination of processes: a
383 modification in the O_3 production rates in the upper stratosphere induced by changes in
384 spectral solar irradiance (e.g. Brasseur et al., 1993), the transport of solar proton event-
385 produced NO_y from the mesosphere down to the mid-low stratosphere where it decreases
386 active chlorine and bromine and, hence, O_3 destruction (e.g. Jackman et al., 2000; Hood
387 and Soukharev, 2006; and references therein) while it enhances the O_3 destruction in the
388 MUST through NO_x catalysed cycles, and its impact on the lower stratospheric dynamics
389 including the QBO (e.g. Hood et al., 1997; Zerefos et al., 1997; Kodera and Kuroda,
390 2002; Hood and Soukharev, 2003, Soukharev and Hood, 2006). As for the QBO, the

391 strong SF dependence at polar latitudes in the LSt with zonal asymmetry in the O₃
392 response reflects the influence of the polar vortex strength and of stratospheric warmings,
393 and are in good agreement with previous results (e.g. Hood et al., 1997; Zerefos et al.,
394 1997; Labitzke and van Loon, 1999; Steinbrecht et al., 2003; Coldewey-Egbers et al.,
395 2014). It is also worth noting that because only one solar cycle is covered, the QBO and
396 SF effects could not be completely separated because they have a strong interaction
397 (McCormack et al., 2007).

398
399 3. EPF - The vertical component of the planetary wave Eliassen-Palm flux entering the
400 lower stratosphere corresponds to the divergence of the wave momentum that drives the
401 meridional residual Brewer-Dobson circulation. In agreement with previous studies (e.g.
402 Fusco and Salby, 1999; Randel et al., 2002; Brunner et al., 2006; Weber et al., 2011),
403 fluctuations in the BDC are shown to cause changes on stratospheric O₃ distribution
404 observed from IASI: EPF largely positively contributes to the LSt O₃ variations at high
405 latitudes of both hemispheres where O₃ is accumulated because of its long chemical
406 lifetime, with amplitude ranging between ~20 and 100 DU (see Fig. 5 and 6; i.e. relative
407 contribution of ~35-150%). The influence of the EPF decreases at lower latitudes where a
408 stronger circulation induces more O₃ transported from the tropics to middle-high latitudes
409 and, hence, a decrease in O₃ levels particularly below 20 km (Brunner et al., 2006). The
410 influence of EP fluxes in the Arctic is the smallest in summer (see Fig.7; <~35 DU vs ~70
411 DU in fall; the two other seasons are not shown) due to the later O₃ build-up in polar
412 vortices. In the S.H., because of the formation of the O₃ hole, the EP influence is smaller
413 than in the N.H. and the seasonal variations are less marked. In the MUST, the O₃
414 response attributed to variations in EPF is positive in both hemispheres, with a much
415 lower amplitude than in the LSt (up to ~20-35 DU). The region of out-of-phase relation
416 with negative EPF coefficients over the high southern latitudes (Fig. 5b) is likely
417 attributable to the influence of VPSC that has correlations with EPF by construction (see
418 Section 2.2). Furthermore, given the annual oscillations in EPF, compensation by the 1-yr
419 harmonic term (eq. 1, Section 2) is found, but it remains weaker than the EPF
420 contribution (data not shown), in particular at high latitudes where the EPF contribution
421 is the largest.

422
423 4. VPSC - Identically to EPF, VPSC is shown to mainly contribute to O₃ variations in LSt
424 over the polar regions (~55 DU or 40% in the N.H. vs ~60 DU or 85% in the S.H. on a
425 longitudinal average; see Fig. 6b) but with an opposite phase (Fig. 5 and 6a). The
426 amplitude of the O₃ response to VPSC reaches its maximum over the southern latitudes
427 during the spring (~60 DU; see Fig.7a for the austral spring period), which is consistent
428 with the role of PSCs on the polar O₃ depletion when there is sufficient sunlight. The
429 strong VPSC influence found at high northern latitudes in fall (Fig. 7a) are due to
430 compensation effects with EPF as pointed out above and verified from sensitivity tests

431 (not shown). Note also that the VPSC contribution into MUST reflects the larger
432 correlation between the two stratospheric layers over the southern polar region (Section
433 2.1, Fig. 1d).

434

435 5. AERO - Five important volcanic eruptions with stratospheric impact occurred during the
436 IASI mission (Kasatochi in 2008, Sarychev in 2009, Nabro in 2011, Sinabung in 2014
437 and Calbuco in 2015; see Fig.3). The two major eruptions of the last decades, El Chichon
438 (1982) and Mt. Pinatubo (1991), which injected sulfur gases into the stratosphere, have
439 been shown to enhance PSCs particle abundances (~15-25 km altitude), to remove NO_x
440 (through reaction with the surface of the sulfuric aerosol to form nitric acid) and, hence,
441 to make the ozone layer more sensitive to active chlorine (e.g. Hofmann et al., 1989;
442 Hofmann et al., 1993; Portmann et al., 1996; Solomon et al., 2016). Besides this chemical
443 effect, the volcanic aerosols also warm the stratosphere at lower latitudes through
444 scattering and absorption of solar radiation, which further induces indirect dynamical
445 effects (Dhomse et al., 2015; Revell et al., 2017). Even though the recent eruptions have
446 been of smaller magnitude than El Chichon and Mt. Pinatubo, they produced sulphur
447 ejection through the tropopause into the stratosphere (see Section 2.2, Fig.2 and Fig.3), as
448 seen with AOD reaching 5×10^{-4} over the stratosphere (150-2 hPa), especially following
449 the eruptions of Nabro (13.3°N, 41.6°E), Sinabung (3.1°N, 98.3°E) and Calbuco (41.3°S,
450 72.6°W). In the LSt, the regression supports an enhanced O₃ depletion over the Antarctic
451 in presence of sulfur gases with a significantly negative annual O₃ response reaching ~25
452 DU (i.e. relative contribution of ~20% into O₃ variation; see Fig. 5b). On the contrary,
453 enhanced O₃ levels in response to sulfuric acid are found in the MUST with a maximum
454 impact of up to 10 DU (i.e. relative contribution of ~20% into the O₃ variation; see Fig.
455 5a) over the Antarctic. The change in phase in the O₃ response to AERO between the LSt
456 (~15-25 km) and the MUST (~25-40 km) over the Antarctic, as well as between polar and
457 lower latitudes in the LSt (see Fig.5 and 6a), agree well with the heterogeneous reactions
458 on sulfuric aerosol surface which reduce the concentration of NO_x to form nitric acid,
459 leading to enhanced O₃ levels above 25 km but leading to decreased O₃ levels due to
460 chlorine activation below 25 km (e.g. Solomon et al., 1996). On a seasonal basis, the
461 depletion due to the presence of sulfur gases reaches ~30 DU on a longitudinal average,
462 over the S.H. polar region during the austral spring (see Fig.7a) highlighting the link
463 between volcanic gases converted to sulfate aerosols and heterogeneous polar halogen
464 chemistry.

465

466 6. NAO – The NAO is an important mode of global climate variability, particularly in
467 northern winter. It describes large-scale anomalies in sea level pressure systems between
468 the sub-tropical Atlantic (Azores; high pressure system) and sub-polar (Iceland; low
469 pressure system) regions (Hurrell, 1995). It disturbs the location and intensity of the
470 North Atlantic jet stream that separates these two regions depending on the phase of

471 NAO. The positive (negative) phase of the NAO corresponds to larger (weaker) pressure
472 difference between the two regions leading to stronger westerlies (easterlies) across the
473 mid-latitudes (Barnston and Livezey, 1987). The two pressure system regions are clearly
474 identified in the stratospheric O₃ response to NAO, particularly in the LSt, with positive
475 regression coefficients above the Labrador-Greenland region and negative coefficients
476 above the Euro-Atlantic region (Fig. 5b). Above these two sectors, the positive phase
477 induces, respectively, an increase and a decrease in LSt O₃ levels. The negative phase is
478 characterized by the opposite behaviour. That NAO pattern is in line with previous
479 studies (Rieder et al., 2013) and was also observed from IASI in tropospheric O₃ (Wespes
480 et al., 2017). The magnitude of annual LSt O₃ changes attributed to NAO variations
481 reaches ~20 DU over the in-phase Labrador region (i.e. contribution of 25% relative to
482 the O₃ variations), while a much lower contribution is found for the MUST (~4 DU or
483 ~10%). The NAO coefficient in the LSt also shows that the influence of the NAO
484 extends further into northern Asia in the case of prolonged NAO phases. The NAO has
485 also been shown to influence the propagation of waves into the stratosphere, hence, the
486 BDC and the strength of the polar vortex in the N.H. mid-winter (Thompson and
487 Wallace, 2000; Schnadt and Dameris, 2003; Rind et al., 2005). That connection between
488 the NAO and the BDC might explain the negative anomaly in the O₃ response to EPF in
489 the LSt over northern Asia which matches the region of negative response to the NAO.

- 490
- 491 7. AAO - The extra-tropical circulation of the S.H. is driven by the Antarctic oscillation that
492 is characterized by geopotential height anomalies south of 20°S, with high anomalies of
493 one sign centered in the polar region and weaker anomalies of the opposing sign north of
494 55°S (Thompson and Wallace, 2000). This corresponds well to the two band-like regions
495 of opposite signs found for the regression coefficients of adjusted AAO in the LSt
496 (negative coefficients centered in Antarctica and positive coefficient north of ~40°S; see
497 Fig.5b). Similarly to the NAO, the strength of the residual mean circulation and of the
498 polar vortex in the S.H. are modulated by the AAO through the atmospheric wave
499 activity (Thompson and Wallace, 2000; Thompson and Solomon, 2001). During the
500 positive (negative) phase of the AAO, the BDC is weaker (stronger) leading to less
501 (more) O₃ transported from the tropics into the southern polar region, and the polar
502 vortex is stronger (weaker) leading to more (less) O₃ depletion inside. This likely
503 explains both the positive AAO coefficients in the region north of ~40°S (contribution <
504 ~5 DU or ~10%) and the negative coefficients around and over the Antarctic
505 (contribution reaching ~10 DU or ~15%; exception is found with positive coefficients
506 over the western Antarctic). The dependence of O₃ variations to the AAO in the MUST is
507 lower than ~7 DU (or ~15%).
- 508
- 509 8. ENSO - Besides the NAO and the AAO, the El Nino southern oscillation is another
510 dominant mode of global climate variability. This coupled ocean-atmosphere

511 phenomenon is governed by sea surface temperature (SST) differences between high
512 tropical and low extra-tropical Pacific regions (Harrison and Larkin, 1998). Domeisen et
513 al. (2019) have recently reviewed the possible mechanisms connecting the ENSO to the
514 stratosphere in the tropics and the extratropics of both hemispheres. The ozone response
515 to ENSO is represented in Fig. 5 only for the ENSO-lag3 proxy which is found to be the
516 main ENSO proxy contributing to the observed O₃ variations. While in the troposphere,
517 previous works have shown that the ENSO influence mainly results in a high contrast of
518 the regression coefficients between western Pacific/Indonesia/North Australia and
519 central/eastern Pacific regions caused by reduced rainfalls and enhanced O₃ precursor
520 emissions above western Pacific (called “chemical effect”) (e.g. e.g. Oman et al., 2013;
521 Valks et al., 2014; Ziemke et al., 2015; Wespes et al., 2016; and references therein), the
522 LSt O₃ response to ENSO is shown here to translate into a strong tropical-extratropical
523 gradient in the regression coefficients with a negative response in the tropics and a
524 positive response at higher latitudes (~5 DU and ~10 DU, respectively, on longitudinal
525 averages; see Fig. 6a). In the MUST, ENSO is globally a smaller out-of-phase driver of O₃
526 variations (response of ~5 DU). The decrease in LSt O₃ during the warm ENSO phase in
527 the tropics (characterized by a negative ENSO lag-3 coefficient reaching 7 DU (or 35%),
528 respectively, in the LSt; see Fig. 5) is consistent with the ENSO-modulated upwelling via
529 deep convection in the tropical lower stratosphere and, hence, increased BD circulation
530 (e.g. Randel et al., 2009). The in-phase accumulation of LSt O₃ in the extra-tropics
531 (contribution reaching 15 DU or 20%; see Fig. 5) is also consistent with enhanced extra-
532 tropical planetary waves that propagate into the stratosphere during the warm ENSO
533 phase, resulting in sudden stratospheric warmings and, hence, in enhanced BDC and
534 weaker polar vortices (e.g. Brönnimann et al., 2004; Manzini et al., 2006; Cagnazzo et
535 al., 2009). The very pronounced link between stratospheric O₃ and the ENSO related
536 dynamical pathways with a time lag of about 3 months is one key finding of the present
537 work. Indeed, the influence of ENSO on stratospheric O₃ measurements has already been
538 reported in earlier studies (Randel and Cobb, 1994; Brönnimann et al., 2004; Randel et
539 al., 2009; Randel and Thompson, 2011; Oman et al., 2013; Manatsa and Mukwada, 2017;
540 Tweedy et al., 2018), but it is the first time that a delayed stratospheric O₃ response is
541 investigated in MLR studies. A 4- to 6-month time lag in O₃ response to ENSO has
542 similarly been identified from IASI in the troposphere (Wespes et al., 2017), where it was
543 explained not only by a tropospheric pathway but also by a specific stratospheric pathway
544 similar to that modulating stratospheric O₃ but with further impact downward onto
545 tropospheric circulation (Butler et al., 2014; Domeisen et al., 2019). Furthermore, the 3-
546 month lag identified in the LSt O₃ response is fully consistent with the modelling work of
547 Cagnazzo et al. (2009) that reports a warming of the polar vortex in February-March
548 following a strong ENSO event (peak activity in November-December) associated with
549 positive O₃ ENSO anomaly reaching ~10 DU in the Arctic and negative anomaly of ~6-7
550 DU in the Tropics. We find that the tropical-extra-tropical gradient in O₃ response to

551 ENSO-lag3 is indeed much stronger in spring with contributions of ~20-30 DU (see
552 Fig.7a for the austral spring period vs winter).

553
554 Overall, although the annual MLR model underestimates the O₃ variability at high latitudes
555 (>50°N/S) by up to 5 DU, particularly in the MUST (see Fig. 6b), we conclude that it gives a
556 good overall representation of the sources of O₃ variability in the two stratospheric layers
557 sounded by IASI. This is particularly true for the spring period (see Fig. 7) which was studied in
558 several earlier works to reveal the onset of Antarctic total O₃ recovery (Salby et al., 2011;
559 Kuttippurath et al., 2013; Shepherd et al., 2014; Solomon et al., 2016; Weber et al., 2018),
560 despite the large O₃ variability due to the hole formation during that period (~80 DU). It is also
561 interesting to see from Fig.7 that the broad O₃ depletion over Antarctica in the LSt is attributed
562 by the MLR to VPSC (up to 60 DU of explained O₃ variability on a latitudinal average).
563 Following these promising results, we further analyze below the O₃ variability in response to
564 anthropogenic perturbations, assumed in the MLR model by the linear trend term, with a focus
565 over the polar regions.

566

567 **4 Trend analysis**

568

569 **4.1 10-year trend detection in stratospheric layers**

570

571 The distributions of the linear trend estimated by the annual regression are represented in Fig. 8a
572 for the MUST and the LSt (left and right panels). In agreement with the early signs of O₃
573 recovery reported for the extra-tropical mid- and upper stratosphere above ~25-10 hPa (>25-30
574 km; Pawson et al., 2014; Harris et al., 2015; Steinbrecht et al., 2017; Sofieva et al., 2017; Ball et
575 al., 2018), the MUST shows significant positive trends larger than 1 DU/yr poleward of ~35°N/S
576 (except over Antarctica). The corresponding decadal trends (>10 DU/decade) are much larger
577 than the discontinuity of ~2-4 DU encountered in the MUST record on 15 September 2010 and
578 discussed in section 2.1. The tropical MUST also shows positive trends but they are weaker (<0.8
579 DU/yr) or not significant. The largest increase is observed in polar O₃ with amplitudes reaching
580 ~2.0 DU/yr. The mid-latitudes also show significant O₃ enhancement which can be attributed to
581 air mass mixing after the disruption of the polar vortex (Knudsen and Grooss, 2000; Fioletov and
582 Shepherd, 2005; Dhomse, 2006; Nair et al., 2015).

583

584 As in the MUST, the LSt is characterized in the southern polar latitudes by significantly positive
585 and large trends (between ~ 1.0 and 2.5 DU/yr). In the mid-latitudes, the lower stratospheric
586 trends are significantly negative, i.e. opposite to those obtained in the MUST. This highlights the
587 independence between the two O₃ layers sounded by IASI in the stratosphere. Poleward of 25°N
588 the negative LSt trends range between ~ -0.5 and -1.7 DU/yr. Negative trends in lower
589 stratospheric O₃ have already been reported in extra-polar regions from other space-based
590 measurements (Kyrölä et al., 2013; Gebhardt et al., 2014; Sioris et al., 2014; Harris et al., 2015;

591 Nair et al., 2015; Vigouroux et al., 2015; Wespes et al., 2016; Steinbrecht et al., 2017; Ball et al.,
592 2018) and may be due to changes in stratospheric dynamics at the decadal timescale (Galytska et
593 al., 2019). These previous studies, which were characterized by large uncertainties or resulted
594 from composite-data merging techniques, are confirmed here using a single dataset. The negative
595 trends which are observed at lower stratospheric middle latitudes are difficult to explain with
596 chemistry-climate models (Ball et al., 2018). It is also worth noting that the significant MUST and
597 LSt O₃ trends are of the same order as those previously estimated from IASI over a shorter
598 period (from 2008 to 2013) and latitudinal averages (see Wespes et al., 2016). This suggests that
599 the trends are not very sensitive to the natural variability in the IASI time series, hence,
600 supporting the significance of the O₃ trends presented here.

601

602 The sensitivity of IASI O₃ to the estimated trend from MLR is further verified in Fig. 8b that
603 represents the global distributions of relative differences in the *RMSE* of the regression residuals
604 obtained with and without a linear trend term included in the MLR model ($(RMSE_{w/o_LT} -$
605 $RMSE_{with_LT})/RMSE_{with_LT} \times 100$; in %). An increase of ~1.0-4.0% and ~0.5-2.0% in the *RMSE*
606 is indeed observed for both the MUST and the LSt, respectively, in regions of significant trend
607 contribution (Fig. 8a), when the trend is excluded. This demonstrates the significance of the
608 trend in improving the performance of the regression. Another statistical method that can be used
609 for evaluating the possibility to infer, from the IASI time period, the significant positive or
610 negative trends in the MUST and the LSt, respectively, consists in determining the expected year
611 when these specified trends would be detectable from the available measurements (with a
612 probability of 90%) by taking into account the variance (σ_ϵ^2) and the autocorrelation (Φ) of the
613 noise residual according to the formalism of Tiao et al. (1990) and Weatherhead et al. (1998).
614 Such a method has already been used for evaluating the trends derived from IASI in the
615 troposphere (Wespes et al., 2018). It represents a more drastic and conservative method than the
616 standard MLR. The results are displayed in Fig. 8c for an assumed specified trend of |1.5| DU/yr,
617 which corresponds to a medium amplitude of trends derived here above from the MLR over the
618 mid-polar regions (Fig. 8a). In the MUST, we find that ~2-3 additional years of IASI
619 measurements would be required to unequivocally detect a trend of |1.5| DU/yr (with probability
620 0.90) over high latitudes (detectable from ~2020-2022 \pm 6-12 months) whereas it should already
621 be detectable over the mid- and lower latitudes (from ~2015 \pm 3-6 months). In the LSt, an
622 additional ~7 years (\pm 1-2 years) of IASI measurements would be required to categorically
623 identify the probable decline derived from the MLR in northern mid-latitudes, and even more to
624 measure the enhancement in the southern polar latitudes. The longer required measurement
625 period at high latitudes is due to the larger noise residuals in the regression fits (i.e. largest σ_ϵ)
626 at these latitudes (see Fig.4 a and b). Note that a larger specified trend amplitude would
627 obviously require a shorter period of IASI measurement. We find that only ~2 additional years
628 would be required to detect a specified trend of |2.5| DU/yr which characterizes the LSt at high
629 latitudes (data not shown).

630

631 **4.2 Stratospheric contributions to total O₃ trend**

632

633 The effect on total O₃ of the counteracting trends in the northern mid-latitudes and of the
634 constructive trends in the southern polar latitudes in the two stratospheric layers sounded by IASI
635 is now investigated.

636

637 Figure 9 represents the global distributions of the contribution of the MUST and the LSt into the
638 total O₃ columns (Fig.9a; in %), of the adjusted trends for the total O₃ (Fig. 9b in DU/yr) and of
639 the estimated year for a |1.5| DU/yr trend detection with a probability of 90% (Fig. 9c). While no
640 significant change or slightly positive trends in total O₃ after the inflection point in 1997 have
641 been reported on an annual basis (e.g; Weber et al., 2018), Fig. 9b shows clear significant
642 changes: negative trend at northern mid- and high latitudes (up to ~2.0 DU/yr north of 30°N) and
643 positive trend over the southern polar region (up to ~3.0 DU/yr south of 45°S). Although
644 counteracting trends between lower and upper stratospheric O₃ have been pointed out in the
645 recent study of Ball et al. (2018) to explain the non-significant recovery in total O₃, we find from
646 IASI a dominance of the LSt decline that translates to negative trends over some regions of the
647 N.H. mid- and high latitudes in TOC (Fig. 9b). This is explained by the contributions of 45-55%
648 from the LSt to the total column, *vs* ~30-40% from the MUST (Fig. 9a) in the mid- and polar
649 regions over the whole year. In addition, the increase in total O₃ at high southern latitudes is
650 dominated by the LSt, although both layers positively contribute around Antarctica, comparing
651 to the trend distributions in Fig. 8. Note that most previous ozone trends studies, including Ball
652 et al. (2018), excluded the polar regions due to limited latitude coverage of some instruments
653 merged in the data composites.

654

655 While the annual MLR shows a significant dominance of LSt trends over MUST trends in the
656 northern mid-latitudes and significant constructive trends in the southern latitudes, total O₃
657 trends are not ascribed with complete confidence according to the formalism of Tiao et al. (1990)
658 and Weatherhead et al. (1998) discussed in Section 4.1. The detectability of a specified trend of
659 |1.5| DU/yr (Fig. 9c), which corresponds to the medium trend derived from MLR in mid-high
660 latitudes of both hemispheres (Fig. 9b), would need several years of additional measurements to
661 be unequivocal from IASI on an annual basis (from ~2022-2024 over the mid-latitudes and from
662 ~2035 over the polar regions). A higher trend amplitude of ~|2.5| DU/yr derived from the MLR
663 would be observable from ~2020-2025 (figure not shown).

664

665 The use of the annual MLR could translate to large systematic uncertainties on trends (implying
666 large σ_ϵ), which induces a longer measurement period required to yield significant trends. These
667 uncertainties could be reduced on a seasonal basis, by attributing different weights to the

668 seasons, which would help in the categorical detection of a specified trend. This is investigated
669 in the subsection below by focusing on the winter and the spring periods.

670

671 **4.3 Trends in spring and winter**

672

673 The reports on early signs of total O₃ recovery (Salby et al., 2011; Kuttippurath et al., 2013;
674 Shepherd et al., 2014; Solomon et al., 2016; Kuttippurath and Nair, 2017; Weber et al., 2018)
675 have all focused on the Antarctic region during spring, when the ozone hole area is at its
676 maximum extent, i.e. the LSt O₃ levels at minimum values. Here we investigate the respective
677 contributions of the LSt and the MUST to the TOC recovery over the Southern latitudes during
678 spring and also during winter when the minima in O₃ levels occur in the MUST (down to ~60 DU
679 in polar regions), in comparison with the Northern latitudes. Figures 10 and 11, respectively,
680 show the S.H. and the N.H. distributions of the estimated trends from seasonal MLR (left panels)
681 and of the corresponding year required for a significant detection of |3.0| DU increase per year
682 (right panels) during their respective winter (JJA and DJF; Fig. 10a and 11a) and spring (SON
683 and MAM; Fig. 10b and 11b) for the total, MUST and LSt O₃ (top, middle and bottom panels,
684 respectively). Fig. 10 a and b clearly show significant positive trends over Antarctica and the
685 southernmost latitudes of the Atlantic and Indian oceans, with amplitudes ranging between ~1-5
686 DU/yr over latitudes south of ~35-40°S in total, MUST and LSt O₃ ($\sim 3.6 \pm 2.7$ DU/yr, $\sim 3.0 \pm 1.3$
687 DU/yr, $\sim 3.6 \pm 3.1$ DU/yr and $\sim 3.7 \pm 1.7$ DU/yr, $\sim 1.3 \pm 0.7$ DU/yr, $\sim 3.7 \pm 1.6$ DU/yr, on spatial
688 averages, respectively over JJA and SON, for the three O₃ columns). These trends over 10 years
689 are much larger than the amplitude of the discontinuity in the MUST time series (section 2.1) and
690 than the trends estimated in Sections 4.1 (see Fig.8 for the MUST and the LSt) and 4.2 (see Fig.9
691 for TOC) over the whole year. In MUST, significant positive trends are observed during each
692 season over the mid- and polar latitudes of both hemispheres (Fig. 10 and 11 for the winter and
693 spring periods; the other seasons are not shown here) but more particularly in winter and in
694 spring where the increase reaches a maximum of ~4 DU/yr. In the LSt, the distributions are more
695 complex: the trends are significantly negative in the mid-latitudes of both hemispheres,
696 especially in winter and in spring of the N.H., while in spring of the S.H., some mid-latitude
697 regions also show near-zero or even positive trends. The southern polar region shows high
698 significant positive trends in winter/spring (see Fig.10). For the total O₃ at mid-high latitudes,
699 given the mostly counteracting trends detected in the LSt and in the MUST and the dominance of
700 the LSt over the MUST (~45-55% from the LSt vs ~30-40% from the MUST into total O₃ over the
701 whole year;), these latitudes are governed by negative trends, especially in spring of the N.H.
702 High significant increases are detected over polar regions in winter/spring of both hemispheres
703 but more particularly in the S.H. where the LSt and MUST trends are both of positive sign.

704

705 The substantial winter/spring positive trends observed in MUST, LSt and total O₃ levels at high
706 latitudes of the S.H. (and of the N.H. for the MUST) are furthermore demonstrated to be
707 detectable from the available IASI measurement period (see Fig. 10, right panels: an assumed

708 increase of $[3.0]$ DU/yr is detectable from 2016 ± 6 months and from 2018 ± 1 year in the MUST
709 and the LSt, respectively). The positive trend of ~ 4 DU/yr measured in polar total O_3 in
710 winter/spring would be observable from $\sim 2018-2020 \pm 1-2$ year and the decline of ~ -3 DU/yr in
711 winter/spring of the N.H. in LSt would be detectable from $\sim 2018-2020 \pm 9$ months (not shown
712 here). Note that the higher negative trends found above the Pacific at highest latitudes (see Fig.
713 10) correspond to the regions with longest required measurement period for significant trend
714 detection and, hence, point to poor regression residuals. About $\sim 50\%$ and $\sim 35\%$ of the
715 springtime MUST and LSt O_3 variations, respectively, are due to anthropogenic factors (estimated
716 by VPSC \times EESC proxy and linear trend in MLR models). This suggests that O_3 changes
717 especially in the LSt are mainly governed by dynamics, which contributes to a later projected
718 trend-detection year in comparison with the MUST (Fig. 10 and 11) and which may hinder the O_3
719 recovery process.

720

721 Overall, the large positive trends estimated concurrently in LSt, MUST and total O_3 over the
722 Antarctic region in winter/spring likely reflect the healing of the ozone layer with a decrease of
723 polar ozone depletion (Salomon et al., 2016) and, hence, demonstrate the efficiency of the
724 Montreal protocol. To the best of our knowledge, these results represent the first detection of a
725 significant recovery in the stratospheric and the total O_3 columns over the Antarctic from one
726 single satellite dataset.

727

728 **4.4 Speeding up in O_3 changes**

729

730 Positive trends in total O_3 have already been determined earlier by Solomon et al. (2016) and by
731 Weber et al. (2018) over Antarctica during September over earlier periods ($\sim 2.5 \pm 1.5$ DU/yr over
732 2000-2014 and $8.2 \pm 6.2\%$ /dec over 2000-2016, respectively). The larger trends derived from the
733 IASI records (see Fig.10b; $\sim 3.7 \pm 1.7$ DU/yr or $\sim 14.4 \pm 5.8\%$ /dec on average in TOC during SON)
734 suggest that the O_3 response could be speeding up due to the accelerating decline of O_3 depleting
735 substances (ODS) resulting from the Montreal Protocol. This has been investigated here by
736 estimating the change in trend in MUST, LSt and total O_3 over the IASI mission. Knowing that
737 the length of the measurement period is an important criterion for reducing systematic errors in
738 the trend coefficient determination (i.e. the specific length of natural mode cycles should be
739 covered to avoid any possible compensation effect between the covariates), the ozone response
740 to each natural driver (including VPSC) taken from their adjustment over the whole IASI period
741 (2008-2017; Section 3, Fig.5) is kept fixed. The linear trend term only is adjusted over variable
742 measurement periods that all end in December 2017, by using a single linear iteratively
743 reweighted least squares regression applied on gridded daily IASI time series, after all the
744 sources of natural variability fitted over the full IASI period are removed (typical examples of
745 linear trend adjustment can be found in the Fig. S2 of the supplementary materials). The
746 discontinuity found in the MUST IASI O_3 records on September 2010 (see Section 2.1) is not
747 taken into account in the regression; hence, it might over-represent the trends estimated over

748 periods that start before the jump (i.e. 2008-2017, 2009-2017, 2010-2017). The zonally averaged
749 results are displayed in Fig. 12 for the statistically significant total, MUST and LSt O₃ trends and
750 their associated uncertainty (accounting for the autocorrelation in the noise residuals; in the 95%
751 confidence level) estimated from an annual regression. Note that the results are only shown for
752 periods starting before 2015 as too short periods induce too large standard errors. In the LSt, a
753 clear speeding up in the southern polar O₃ recovery is observed with amplitude ranging from
754 $\sim 1.5 \pm 0.4$ DU/yr over 2008-2017 to $\sim 5.5 \pm 2.5$ DU/yr over 2015-2017 on zonal averages.
755 Similarly, a speeding of the O₃ decline at northern mid-latitudes is found with values ranging
756 between $\sim -0.7 \pm 0.2$ DU/yr over 2008-2017 and $\sim -2.8 \pm 1.2$ DU/yr over 2015-2017. In the MUST, a
757 weaker increase is observed over the year around $\sim 60^\circ$ latitude of the S.H. (from $\sim 0.8 \pm 0.2$ DU/yr
758 over 2008-2017 to $\sim 2.5 \pm 1.3$ DU/yr over 2015-2017). Given the positive acceleration in both LSt
759 and MUST O₃ in the S.H., this is where the total O₃ record is characterized by the largest
760 significant recovery (from $\sim 1.7 \pm 0.7$ DU/yr over 2008-2017 to $\sim 8.0 \pm 3.5$ DU/yr over 2015-2017).
761 Surprisingly, the speeding up in the O₃ decline in the N.H. is more pronounced in the total O₃
762 (from $\sim -1.0 \pm 0.4$ DU/yr over 2008-2017 to $\sim -5.0 \pm 2.5$ DU/yr over 2015-2017) compared to the
763 LSt, despite the opposite trend in MUST O₃. This could reflect the O₃ decline observed in the
764 northern latitudes in the troposphere (~ -0.5 DU/yr over 2008-2016; cfr Wespes et al., 2018)
765 which is included in the total column.

766
767 Overall, the larger annual significant trend amplitudes derived over the last few years of total,
768 MUST and LSt O₃ measurements, compared with those derived from the whole studied period
769 (Sections 4.1 and 4.2) and from earlier studies, translate to trends that remain detectable over the
770 increasing uncertainty associated to the shorter and shorter time segments (see Fig. S3 of the
771 supplementary materials), especially in both LSt and total O₃ in the S.H. This demonstrates that
772 we progress towards a significant emergence and speeding up of O₃ recovery process in the
773 stratosphere over the whole year. Nevertheless, we calculated that additional years of IASI
774 measurements would help in confirming the changes in O₃ recovery and decline over the IASI
775 period (e.g. ~ 4 additional years are required to verify the trends calculated over the 2015-2017
776 segment in the highest latitudes in LSt). In addition, a longer measurement period would be
777 useful to derive trends over successive segments of same length that are long enough to reduce
778 the uncertainty, in order to make the trend and its associated uncertainty more comparable across
779 the fit.

780

781 **5 Summary and conclusion**

782

783 In this study, we have analysed the changes in stratospheric O₃ levels sounded by IASI-A by
784 examining the global pictures of natural and anthropogenic sources of O₃ changes independently
785 in the lower (150-25 hPa) and in the mid-upper stratosphere (<25 hPa). We have exploited to that
786 end a multi-linear regression model that has been specifically developed for the analysis of
787 stratospheric processes by including a series of drivers known to have a causal relationship to

788 natural stratospheric O₃ variations, namely SF, QBO-10, QBO-30, NAO, AAO, ENSO, AERO,
789 EPF and VPSC. We have first verified the representativeness of the O₃ response to each of these
790 natural drivers and found for most of them characteristic patterns that are in line with the current
791 knowledge of their dynamical influence on O₃ variations. One of the most important finding
792 related to the O₃ driver analysis relied on the detection of a very clear time lag of 3 months in the
793 O₃ response to ENSO in the LSt, with a pronounced contrast between an in-phase response in the
794 extra-tropics and an out-of-phase response in the tropics, which is consistent with the ENSO-
795 modulated dynamic. The 3-month lag observed in the lower stratosphere is also coherent with
796 the 4- to -6 months lag detected from a previous study in the troposphere (Wespes et al., 2017)
797 and further supports the stratospheric pathway suggested in Butler et al. (2014) to explain an
798 ENSO influence over a long distance. The representativeness of the influence of the O₃ drivers
799 was also confirmed on a seasonal basis (e.g. high ENSO-lag3 effect in spring, strong VPSC and
800 AERO influences during the austral spring ...). These results have verified the performance of
801 the regression models (annual and seasonal) to properly discriminate between natural and
802 anthropogenic drivers of O₃ changes. The anthropogenic influence has been evaluated with the
803 linear trend adjustment in the MLR. The main results are summarized as follows:

- 804
- 805 (i) A highly probable (within 95%) recovery process is derived from the annual MLR at high
806 southern latitudes in the two stratospheric layers and, therefore, in the total column. It
807 is also derived at high northern latitudes in the MUST. However, a longer period of
808 IASI measurements is needed to unequivocally demonstrate a positive trend on
809 annual basis in the IASI record. Only ~2-3 additional years of IASI measurements are
810 required in the MUST.
 - 811
 - 812 (ii) A likely O₃ decline (within 95%) is measured in the lower stratosphere at mid-latitudes,
813 specifically, of the N.H., but it would require an additional ~7 years of IASI
814 measurements to be categorically confirmed. Given the large contribution from the
815 LSt to the total column (~45-50% from LSt vs ~35% from the MUST into TOCs), the
816 decline is also calculated in total O₃ with ~4-6 years of additional measurements for
817 the trend to be unequivocal.
 - 818
 - 819 (iii) A significant O₃ recovery is categorically found in the two stratospheric layers
820 (>~35°N/S in the MUST and >~45°S in the LSt) as well as in the total column
821 (>~45°S) during the winter/spring period, which confirms previous studies that
822 showed healing in the Antarctic O₃ hole with a decrease of its areal extent. These
823 results verify the efficacy of the ban on O₃ depleting substances imposed by the
824 Montreal protocol and its amendments, throughout the stratosphere and in the total
825 column, from only one single satellite dataset for the first time.
 - 826

827 (iv) The decline observed in LSt O₃ at northern mid-latitudes is unequivocal over the
828 available IASI measurements in winter/spring of the N.H. The exact reasons for that
829 decline are still unknown but O₃ changes in the LSt are estimated to be mainly
830 attributable to dynamics which likely perturbs the healing of LSt and total O₃ in the
831 N.H.

832
833 (v) A significant speeding up (within 95%) in that decline is measured in LSt and total O₃
834 over the last 10 years (from $\sim -0.7 \pm 0.2$ DU/yr over 2008-2017 to $\sim -2.8 \pm 1.2$ DU/yr
835 over 2015-2017 in LSt O₃ on zonal averages). Even if the acceleration cannot be
836 categorically confirmed yet, it is of particular urgency to understand its causes for
837 apprehending its possible impact on the O₃ layer and on future climate changes.

838
839 (vi) A clear and significant speeding up (within 95%) in stratospheric and total O₃ recovery
840 is measured at southern latitudes (e.g. from $\sim 1.5 \pm 0.4$ DU/yr over 2008-2017 to
841 $\sim 5.5 \pm 2.5$ DU/yr over 2015-2017 in the LSt), which translate to trend values that
842 would be categorically detectable in the next few years on an annual basis. It
843 demonstrates that we are currently progressing towards a substantial emergence in O₃
844 healing in the stratosphere over the whole year in the S.H..

845
846 Additional years of IASI measurements that will be provided by the operational IASI-C (2018)
847 on flight and the upcoming IASI-Next Generation (IASI-NG) instrument onboard the Metop
848 Second Generation (Metop-SG) series of satellites would be of particular interest to confirm and
849 monitor, in the near future and over a longer period, the speeding up in the O₃ healing of the S.H.
850 as well as in the LSt O₃ decline measured at mid-latitudes of the N.H. IASI-NG/Metop-SG is
851 expected to extend the data record much further in the future (Clerbaux and Crevoisier, 2013;
852 Crevoisier et al., 2014).

853

854 **Data availability**

855

856 The IASI O₃ data processed with FORLI-O₃ v0151001 can be downloaded from the Aeris portal
857 at: <http://iasi.aeris-data.fr/O3/> (last access: 14 July 2019).

858

859 **Author contribution**

860

861 C.W. performed the analysis, wrote the manuscript and prepared the figures. D.H. was
862 responsible for the retrieval algorithm development and the processing of the IASI O₃ dataset.
863 All authors contributed to the analysis and reviewed the manuscript.

864

865 **Competing interests**

866

867 The authors declare that they have no conflict of interest.

868

869 **Acknowledgments**

870

871 IASI has been developed and built under the responsibility of the Centre National d'Etudes
872 Spatiales (CNES, France). It is flown onboard the Metop satellites as part of the EUMETSAT
873 Polar System. The IASI L1 data are received through the EUMETCast near real time data
874 distribution service. We acknowledge the financial support from the ESA O₃-CCI and
875 Copernicus O₃-C3S projects. FORLI-O₃ is being implemented at Eumetsat with the support of
876 the AC SAF project. The research in Belgium is also funded by the Belgian State Federal Office
877 for Scientific, Technical and Cultural Affairs and the European Space Agency (ESA Prodex IASI
878 Flow and B-AC SAF). We acknowledge Ingo Wohltmann (Alfred Wagner Institute, Postdam,
879 Germany) as well as Beiping Luo (Institute for Atmosphere and Climate, ETH Zurich,
880 Switzerland) and Larry Thomason (NASA Langley Research Center, Hampton, USA), for
881 processing and providing datasets of volume of polar stratospheric clouds and of sulfuric acid
882 extinction coefficients, respectively. We are also grateful to Maxime Prignon (Université de
883 Liège, Liège, Belgium) for providing several years of BASCOE simulations.

884

885

886

887

888

889

890

891

892

893

894

895

896

897

898

899

900

901

902

903

904

905

906

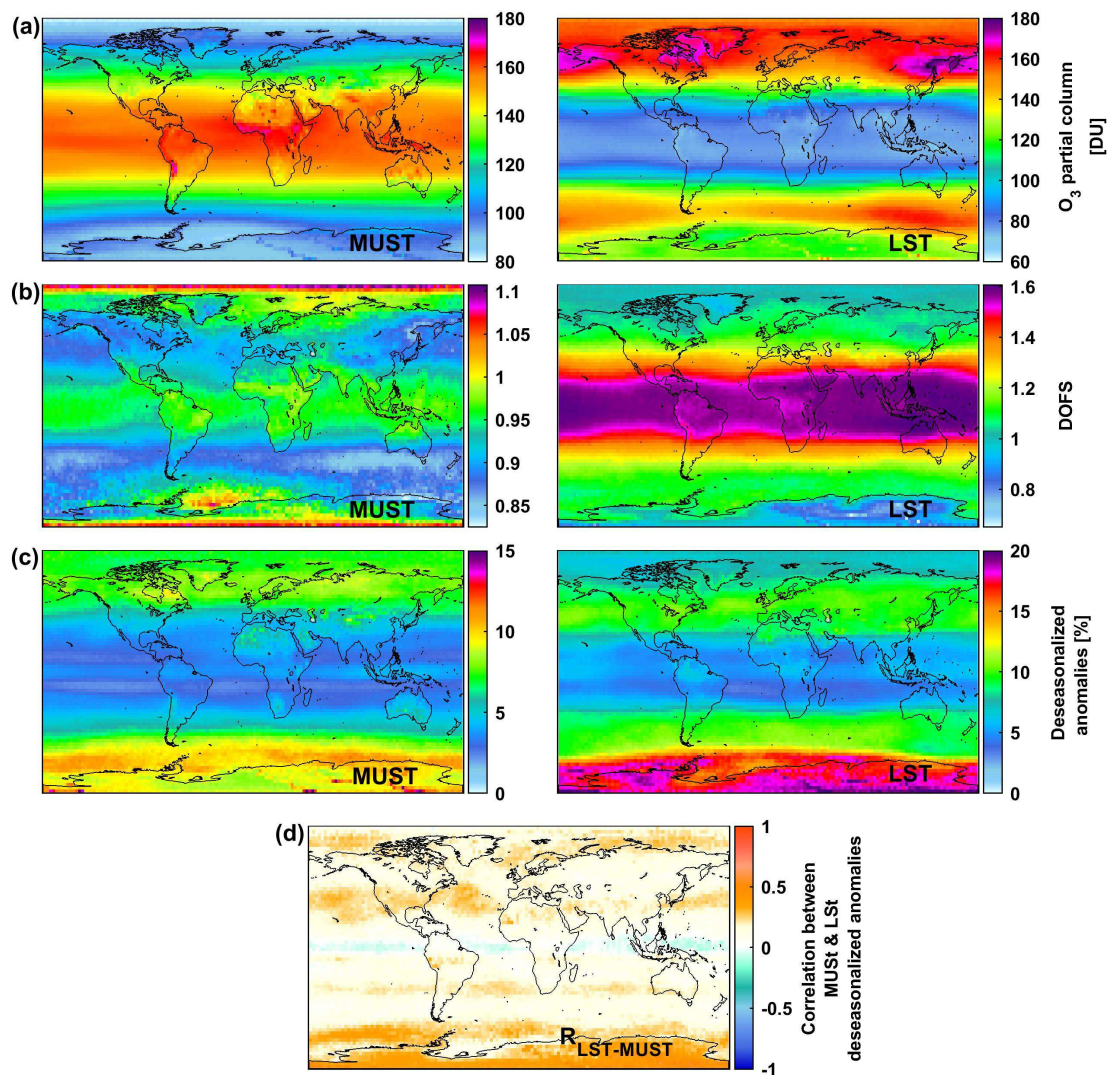
907 **Table 1** List of the explanatory variables used in the multi-linear regression model applied on
 908 IASI stratospheric O₃, their temporal resolution and their sources.
 909

Proxy	Description (<i>resolution</i>)	Sources
F10.7	The 10.7 cm solar radio flux (<i>daily</i>)	NOAA National Weather Service Climate Prediction Center: ftp://ftp.ngdc.noaa.gov/STP/space-weather/solar-data/solar-features/solar-radio/noontime-flux/penticton/penticton_adjusted/listings/listing_drao_noontime-flux-adjusted_daily.txt
QBO¹⁰ QBO³⁰	Quasi-Biennial Oscillation index at 10hPa and 30hPa (<i>monthly</i>)	Free University of Berlin: www.geo.fu-berlin.de/en/met/ag/strat/produkte/qbo/
EPF	Vertical component of Eliassen-Palm flux crossing 100 hPa, averaged over 45°-75° for each hemisphere and accumulated over the 3 or 12 last months depending on the time period and the latitude (see text for more details) (<i>daily</i>)	Calculated at ULB from the NCEP/NCAR gridded reanalysis: https://www.esrl.noaa.gov/psd/data/gridded/data.ncep.reanalysis.html
AERO	Stratospheric volcanic aerosols; Vertically integrated sulfuric acid extinction coefficient at 12 μm over 150-25 hPa and 25-2hPa, averaged over the tropics and the extra-tropics north and south (see text for more details) (<i>monthly</i>)	Extinction coefficients processed at the Institute for Atmosphere and Climate (ETH Zurich, Switzerland; Thomason et al., 2018)
VPSC	Volume of Polar Stratospheric Clouds for the N.H. and the S.H. multiplied by the equivalent effective stratospheric chlorine (EESC) and accumulated over the 3 or 12 last months (see text for details) (<i>daily</i>)	Processed at the Alfred Wagner Institute (AWI, Postdam, Germany; Ingo Wolthmann, private communication) EESC taken from the Goddard Space Flight Center: https://acd-ext.gsfc.nasa.gov/Data_services/automailer/index.html
ENSO	Multivariate El Niño Southern Oscillation Index (MEI) (2- <i>monthly averages</i>)	NOAA National Weather Service Climate Prediction Center: http://www.esrl.noaa.gov/psd/enso/mei/table.html
NAO	North Atlantic Oscillation index for the N.H. (<i>daily</i>)	ftp://ftp.cpc.ncep.noaa.gov/cwlinks/norm.daily.nao.index.b500101.curent.ascii
AAO	Antarctic Oscillation index for the S.H. (<i>daily</i>)	ftp://ftp.cpc.ncep.noaa.gov/cwlinks/norm.daily.aao.index.b790101.curent.ascii
GEO	Geopotential height at 200 hPa (2.5°x2.5° gridded) (<i>daily</i>)	http://apps.ecmwf.int/datasets/data/interim-full-daily/?levtype=pl
PV	Potential vorticity at 200 hPa (2.5°x2.5° gridded) (<i>daily</i>)	

910 **Figure captions**

911

912

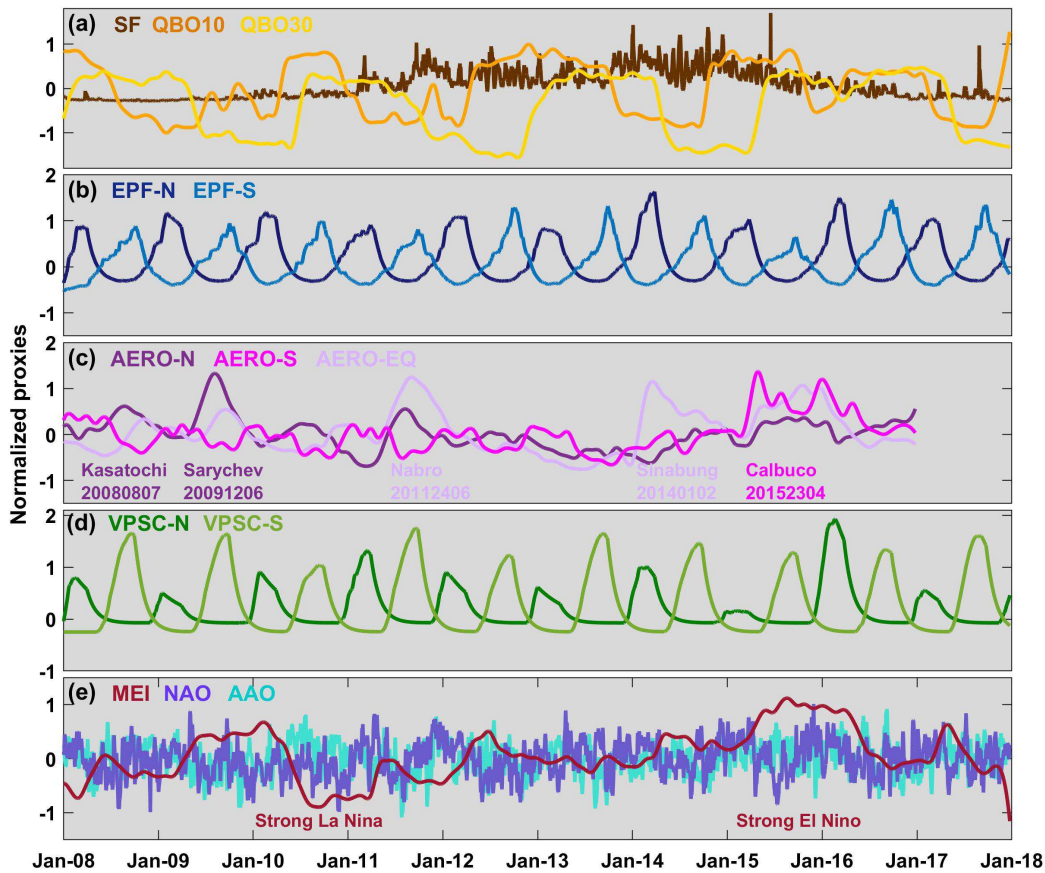


913

914 **Fig.1.** Global distribution of (a) daily O₃ columns (in Dobson Units - DU), (b) associated DOFS,
915 (c) absolute deseasonalized anomalies (in %) averaged over January 2008 – December 2017 in
916 the MUST (Mid-Upper Stratosphere: >25 hPa; left panels) and in the LSt (Lower Stratosphere:
917 150-25hPa; right panels). (d) shows the correlation coefficients between the daily O₃
918 deseasonalized anomalies in the MUST and in the LSt. Note that the scales are different between
919 MUST and LSt.

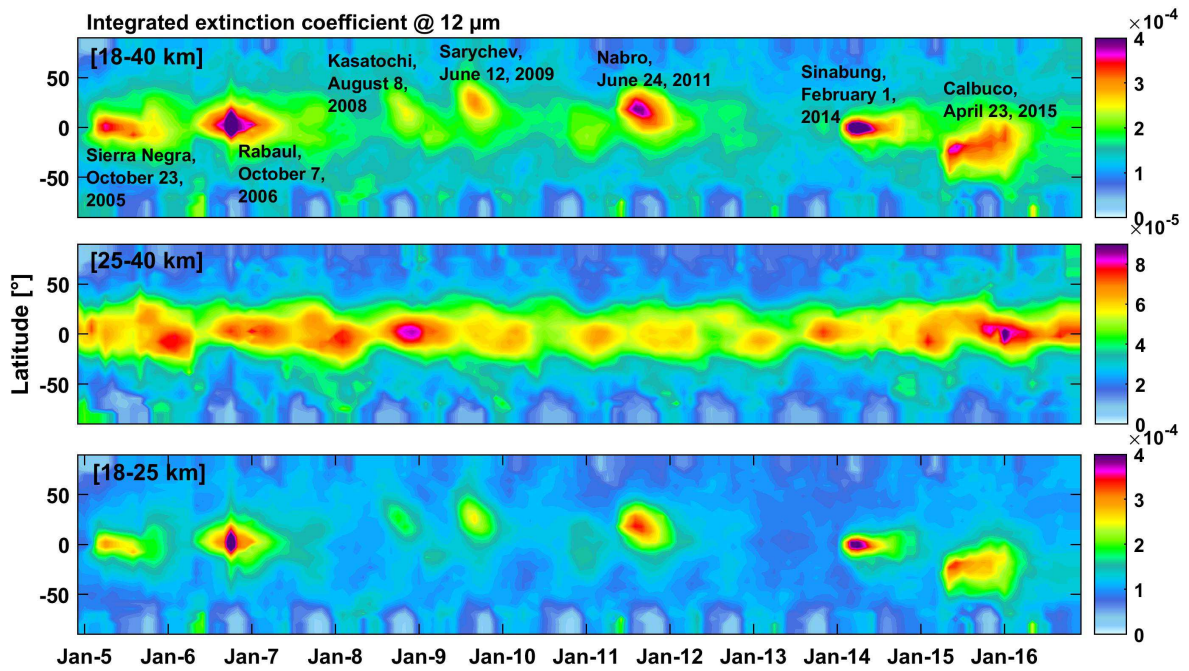
920

921



922
 923
 924
 925
 926
 927
 928
 929
 930
 931
 932
 933
 934
 935
 936

Fig.2. Normalized proxies as a function of time for the period covering January 2008 to December 2017 for (a) the F10.7 cm solar radio flux (SF) and the equatorial winds at 10 (QBO10) and 30 hPa (QBO30), respectively, (b) the upward components of the EP flux crossing 100 hPa accumulated over time and averaged over the 45°-75° latitude band for each hemispheres (EPF-N and EPF-S), (c) the extinction coefficients at 12 μm vertically integrated over the stratospheric O₃ column (from 150-2hPa) and averaged over the extra-tropics north and south (22.5°-90°N/S; AERO-N and AERO-S) and over the tropics (22.5°S-22.5°N; AERO-EQ) (the main volcanic eruptions are indicated), (d) the volume of polar stratospheric clouds multiplied by the equivalent effective stratospheric chlorine (EESC) and accumulated over time for the north and south hemispheres (VPSC-N and VPSC-S) and (e) the El Niño Southern (ENSO), North Atlantic (NAO) and Antarctic (AAO) oscillations.

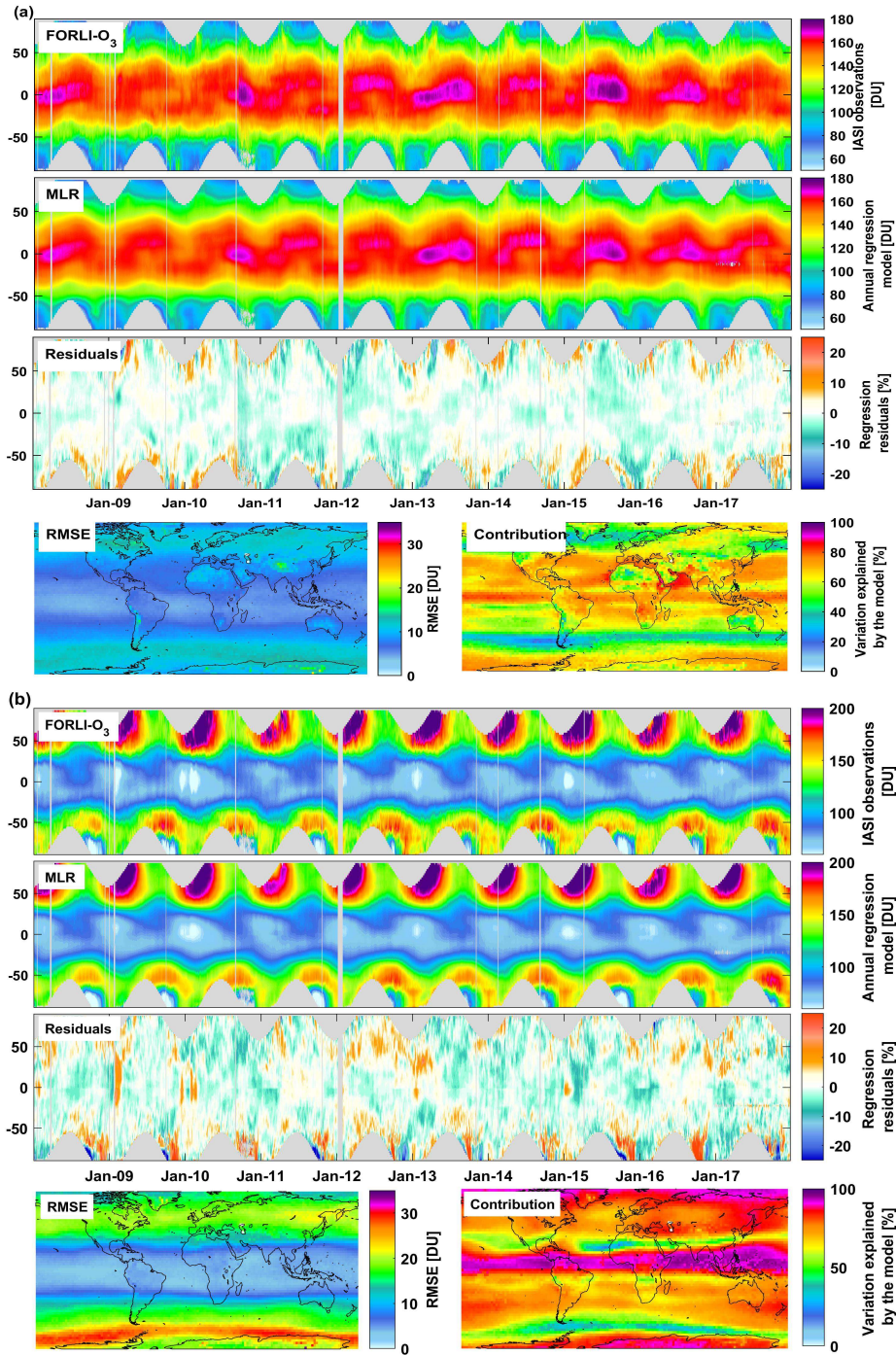


937
938

939 **Fig.3:** Latitudinal distribution of volcanic sulfuric acid extinction coefficient at 12 μm integrated
 940 over the stratosphere (top panel), over the middle stratosphere (middle panel) and the lower
 941 stratosphere (bottom panel) as a function of time from 2005 to 2017. The dataset consists of
 942 monthly mean aerosol data merged from SAGE, SAM, CALIPSO, OSIRIS, 2D-model-
 943 simulation and Photometer (processed at NASA Langley Research Center, USA and ETH
 944 Zurich, Switzerland).

945
946
947
948
949
950
951
952
953
954
955
956
957
958
959
960
961

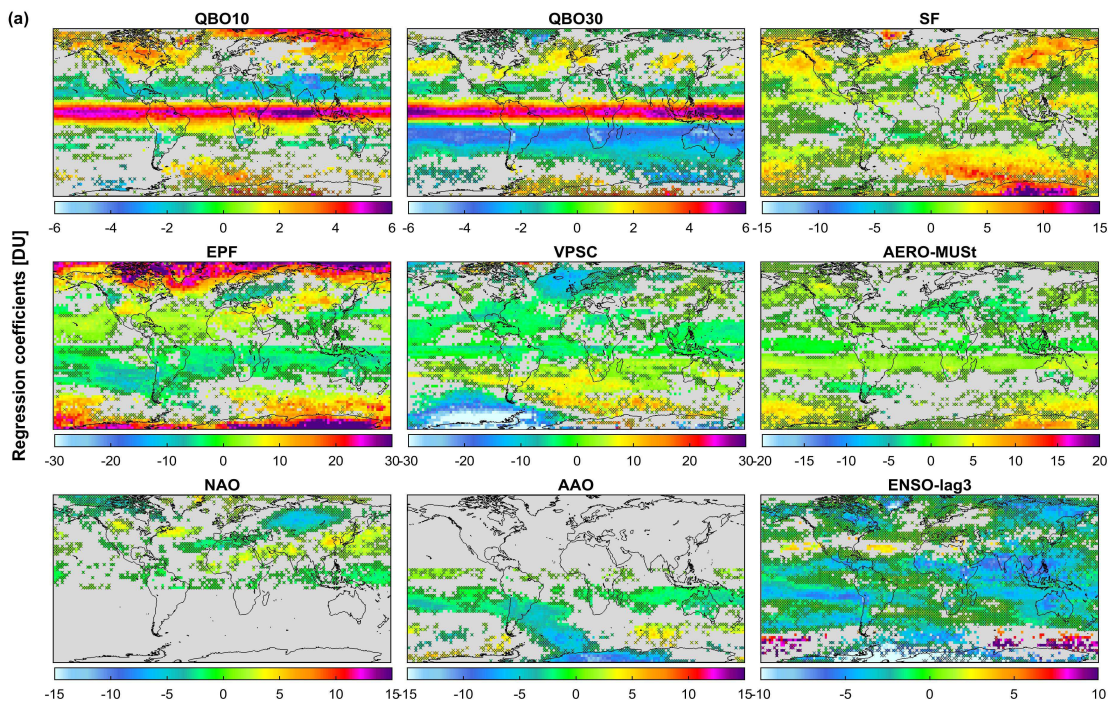
962



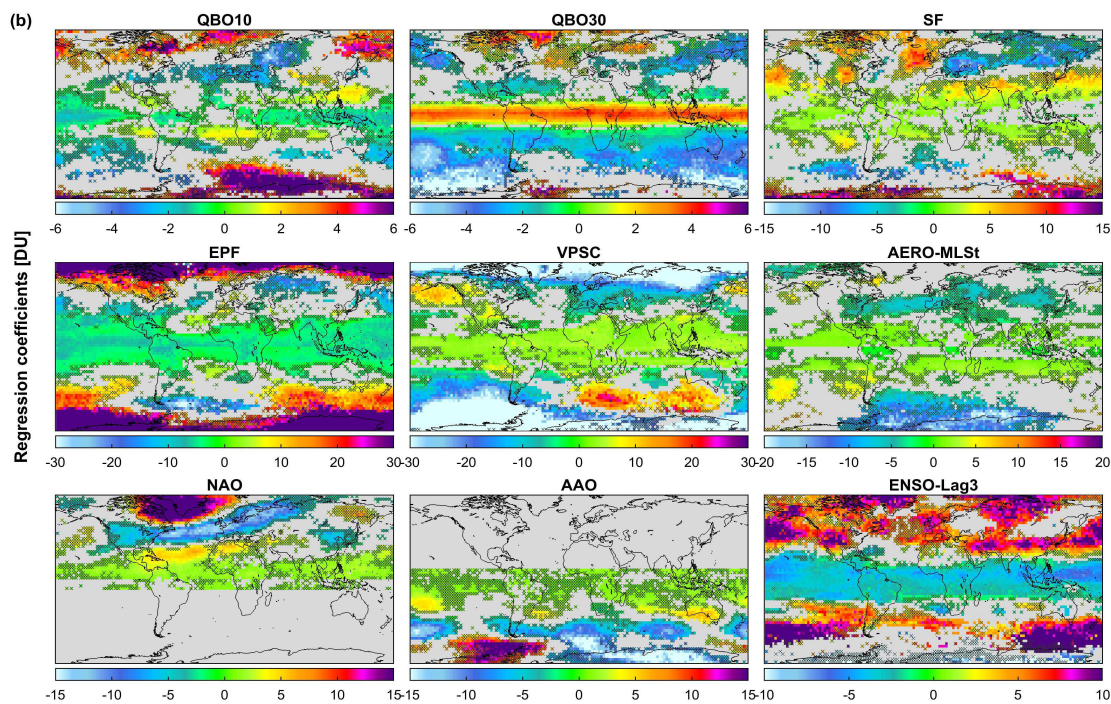
963
964

965 **Fig.4:** Latitudinal distribution of (a) MUST O₃ column and (b) LSt O₃ columns as a function of
 966 time observed from IASI (in DU; top panels), simulated by the annual regression model (in DU,
 967 second panels) and of the regression residuals (in %; third panels). Global distribution of *RMSE*
 968 of the regression residual (in DU) and fraction of the variation in IASI data explained by the
 969 regression model calculated as $[100 \times (\sigma(O_3^{Fitted_model}(t)) / \sigma(O_3(t)))]$ (in %; fourth panels).

970

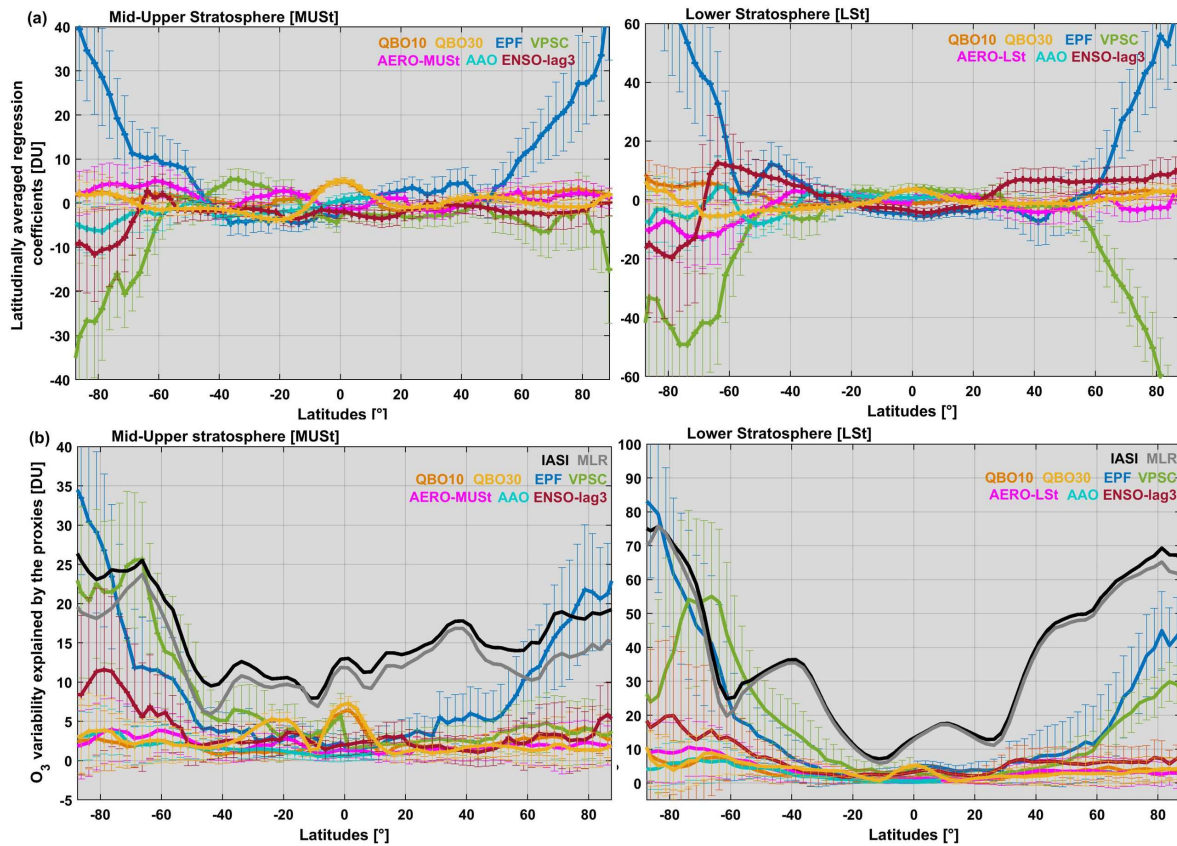


971



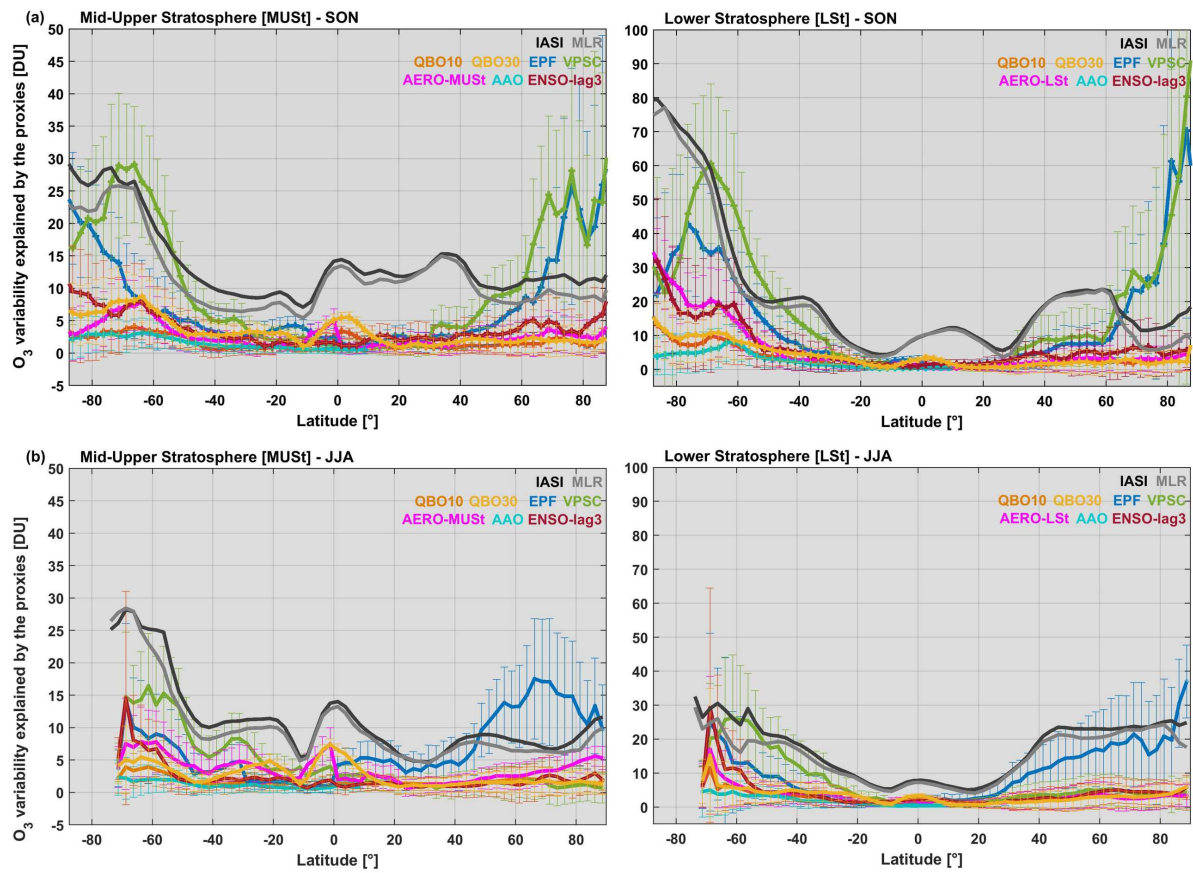
972

973 **Fig.5:** Global distribution of the annual regression coefficient estimates (in DU)
 974 drivers in (a) MUST and in (b) LSt: QBO10, QBO30, SF, EPF, VPSC, AERO, NAO, AAO and
 975 ENSO (ENSO-lag3 for both LSt and MUST). Grey areas and crosses refer to non-significant grid
 976 cells in the 95% confidence limit. Note that the scales differ among the drivers.



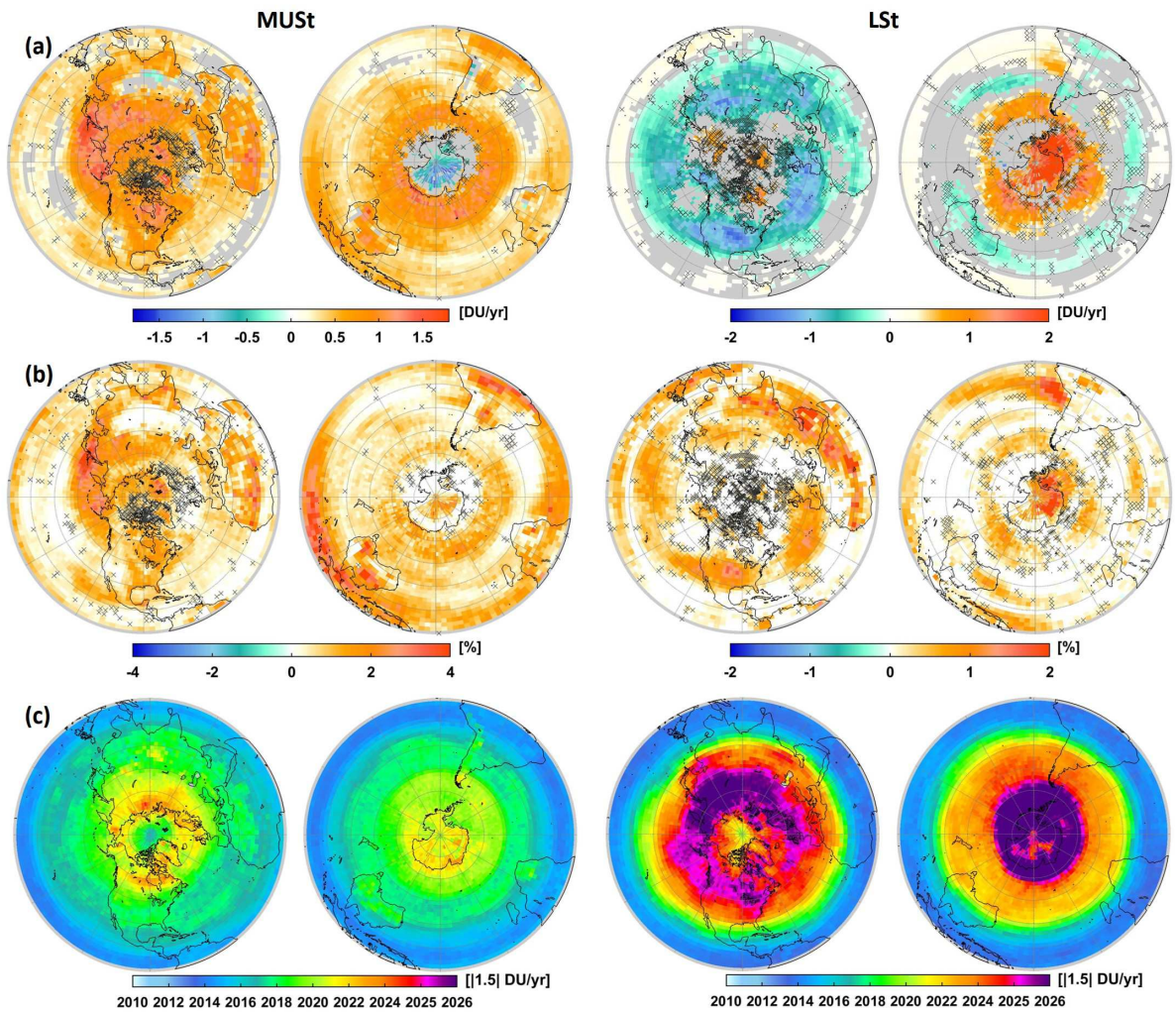
977
 978
 979
 980
 981
 982
 983
 984
 985
 986
 987
 988
 989

Fig.6: Latitudinal distributions (a) of fitting regression coefficients for various O₃ drivers (QBO10, QBO30, EPF, VPSC, AERO, AAO and ENSO-lag3; in DU) and (b) of 2σ O₃ variability due to variations in those drivers (in DU) from the annual MLR in MUST and LSt (left and right panels respectively). Vertical bars correspond (a) to the uncertainty of fitting coefficients at the 2σ level and (b) to the corresponding error contribution into O₃ variation. Note that the scales are different.



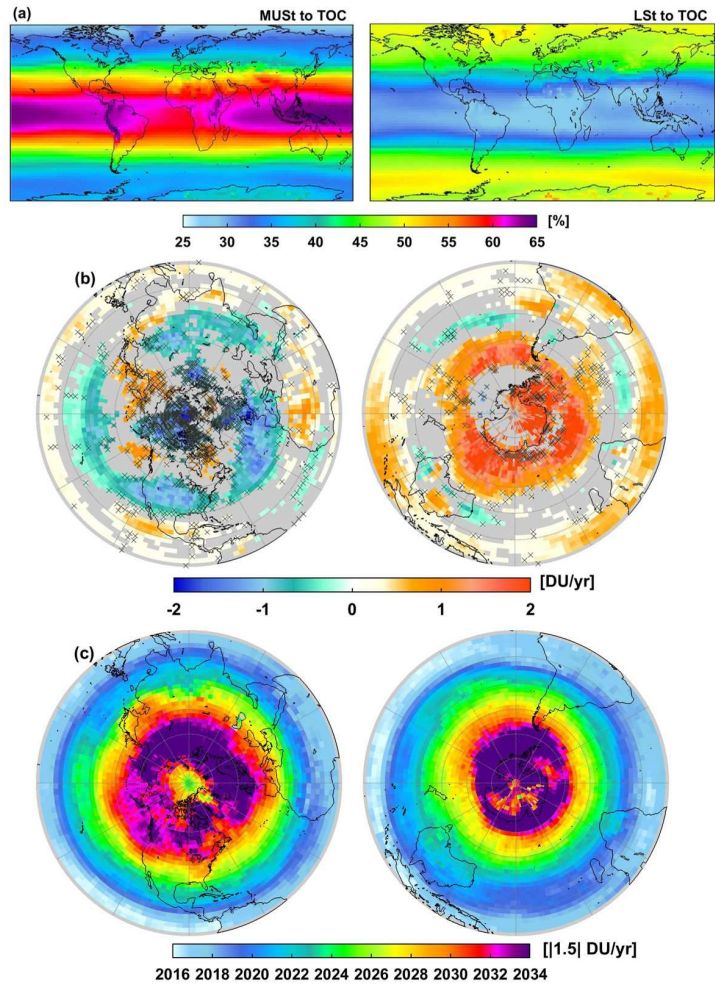
990
 991
 992
 993
 994
 995

Fig.7: Same as Fig. 6b but for (a) the austral winter and (b) the austral spring periods (JJA and SON, respectively) from the seasonal MLR. Note that the scales are different.



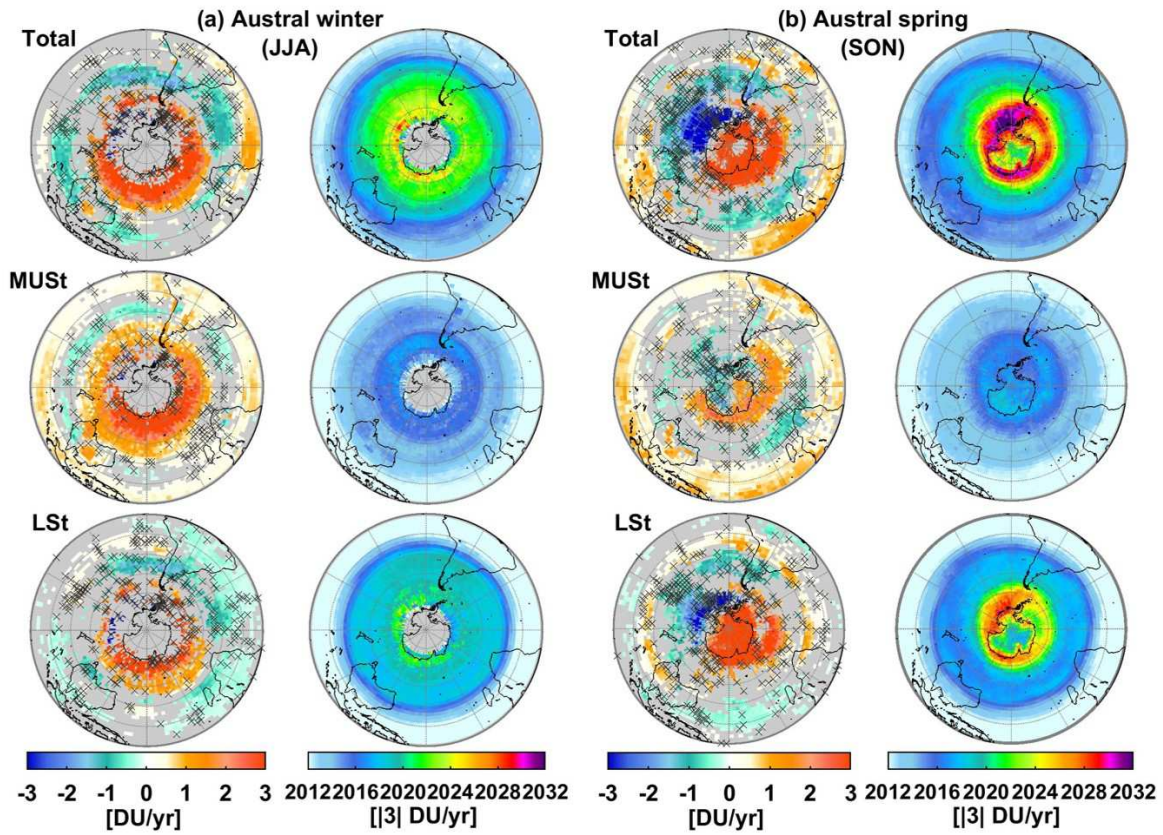
996
 997
 998
 999
 1000
 1001
 1002
 1003
 1004
 1005

Fig. 8: Global distribution (a) of the estimated annual trends (in DU/yr; grey areas and crosses refer to non-significant grid cells in the 95% confidence limit), (b) of the IASI sensitivity to trend calculated as the differences between the *RMSE* of the annual MLR fits with and without linear trend term $[(RMSE_{w/o_LT} - RMSE_{with_LT})/RMSE_{with_LT} \times 100]$ (in %), (c) of the estimated year for a significant detection (with a probability of 90%) of a given trend of $|1.5|$ DU/yr starting in January 2008 in MUST and LSt O₃ columns (left and right panels, respectively). Note that the scales are different for the two layers.



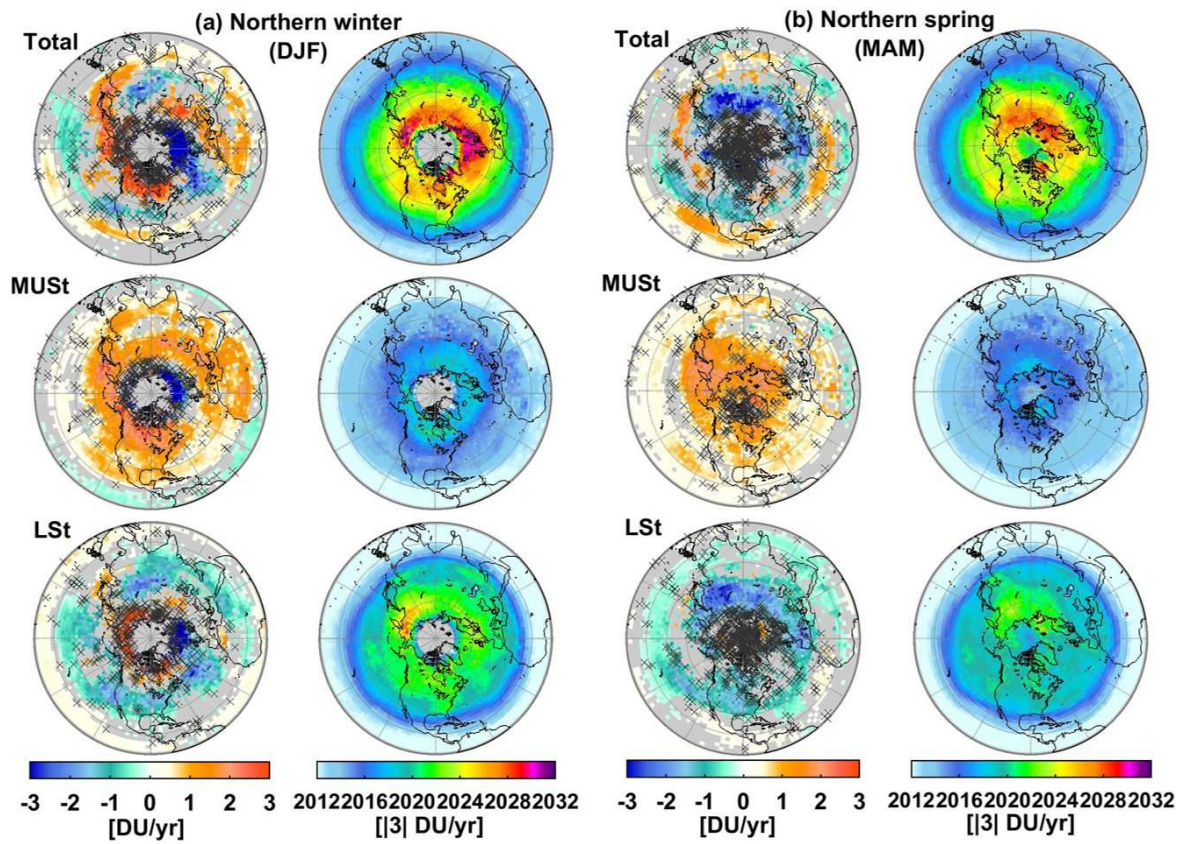
1006
 1007
 1008
 1009
 1010
 1011
 1012

Fig.9: Global distribution of (a) the contribution (in %) of MUST and LSt into the total O₃ (left and right panels respectively) averaged over January 2008 – December 2017, (b) fitted trends in total O₃ (in DU/yr; the grey areas and crosses refer to the non-significant grid cells in the 95% confidence limit) and (c) estimated year for the detection of a significant trend in total O₃ (with a probability of 90%) for a given trend of |1.5| DU/yr starting on January 2008.



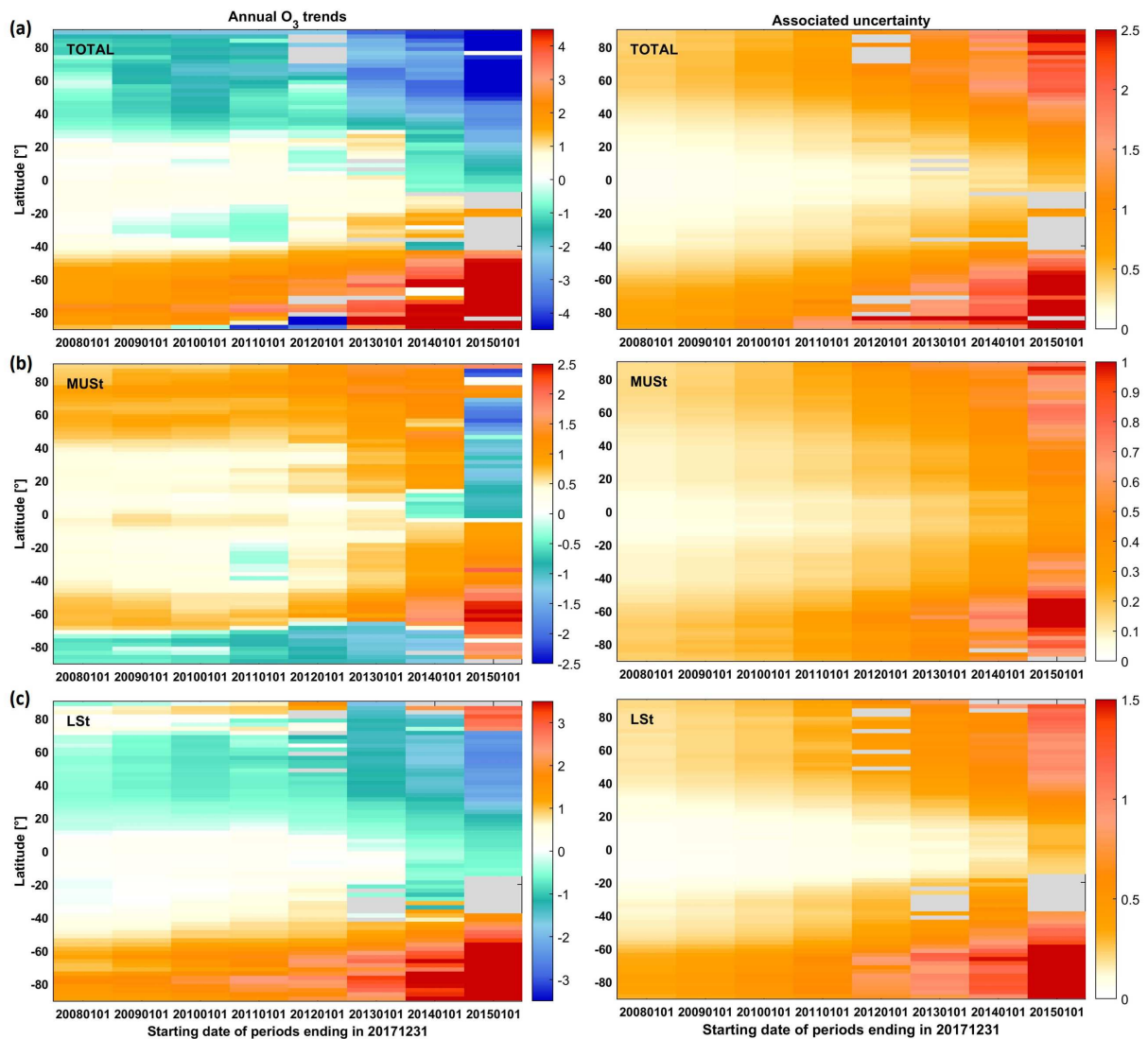
1013
 1014
 1015
 1016
 1017
 1018
 1019
 1020
 1021
 1022
 1023
 1024
 1025
 1026
 1027
 1028
 1029
 1030
 1031

Fig.10: Hemispheric distribution (a) in austral winter (JJA) and (b) in austral spring (SON) of the estimated trends in total, MUS_t and L_{St} O₃ columns (left panels: top, middle and bottom, respectively; in DU/yr; the grey areas and crosses refer to the non-significant grid cells in the 95% confidence limits) and of the corresponding estimated year for a significant trend detection (with a probability of 90%) of a given trend of $|3|$ DU/yr starting at January 2008 (right panels: top, middle and bottom, respectively).



1032
 1033
 1034
 1035
 1036
 1037
 1038

Fig. 11: Same as Fig. 10 but (a) for the winter (DJF) and (b) for the spring (MAM) of the northern Hemisphere.



1039
 1040 **Fig.12:** Evolution of estimated linear trend (DU/yr) and associated uncertainty accounting for the
 1041 autocorrelation in the noise residuals (DU/yr; in the 95% confidence level) in (a) total, (b) MUSSt
 1042 and (c) LSt O₃ columns, as a function of the covered IASI measurement period ending in
 1043 December 2017, with all natural contributions estimated from the whole IASI period (2008-
 1044 2017). Note that the scales are different between the columns.

1045
 1046
 1047
 1048
 1049
 1050
 1051
 1052

1053 **References**

1054

1055 Anderson, J., Russell, J. M., Solomon, S., and Deaver, L. E.: Halogen Occultation Experiment
1056 confirmation of stratospheric chlorine decreases in accordance with the Montreal Protocol, *J.*
1057 *Geophys. Res.-Atmos.*, 105, 4483–4490, <https://doi.org/10.1029/1999JD901075>, 2000.

1058

1059 Baldwin, M. P., L.J. Gray, T.J. Dunkerton, K. Hamilton, P.H. Haynes, W.J. Randel, J.R. Holton,
1060 M.J. Alexander, I. Hirota, T. Horinouchi, D.B.A. Jones, J.S. Kinnersley, C. Marquardt, K. Sato,
1061 and M. Takahashi: The quasi-biennial oscillation, *Rev. Geophys.*, 39, 179–230,
1062 doi:10.1029/1999RG000073, 2001.

1063

1064 Ball, W. T., Alsing, J., Mortlock, D. J., Staehelin, J., Haigh, J. D., Peter, T., Tummon, F., Stübi,
1065 R., Stenke, A., Anderson, J., Bourassa, A., Davis, S. M., Degenstein, D., Frith, S., Froidevaux,
1066 L., Roth, C., Sofieva, V., Wang, R., Wild, J., Yu, P., Ziemke, J. R., and Rozanov, E. V.:
1067 Evidence for a continuous decline in lower stratospheric ozone offsetting ozone layer recovery,
1068 *Atmos. Chem. Phys.*, 18, 1379–1394, <https://doi.org/10.5194/acp-18-1379-2018>, 2018.

1069

1070 Barnston, A. G. and Livezey, R. E.: Classification, seasonality and persistence of low-frequency
1071 atmospheric circulation patterns, *Mon. Weather. Rev.* 115: 1083–1126, 1987.

1072

1073 Boynard, A., D. Hurtmans, K. Garane, F. Goutail, J. Hadji-Lazaro, M. E. Koukouli, C. Wespes,
1074 C. Vigouroux, A. Keppens, J.-P. Pommereau, A. Pazmino, D. Balis, D. Loyola, P. Valks, R.
1075 Sussmann, D. Smale, P.-F. Coheur and C. Clerbaux: Validation of the IASI FORLI/Eumetsat O₃
1076 products using satellite (GOME-2), ground-based (Brewer-Dobson, SAOZ, FTIR) and
1077 ozonesonde measurements, *Atmos. Meas. Tech.*, 11, 5125–5152, 2018.

1078

1079 Brasseur, G.: The response of the middle atmosphere to long-term and short-term solar
1080 variability: A two-dimensional model, *J. Geophys. Res.*, 98, 23 079–23 090, 1993.

1081

1082 Brönnimann, S., Luterbacher, J., Staehelin, J., Svendby, T. M., Hansen, G., and Svenøe, T.:
1083 Extreme climate of the global troposphere and stratosphere 1940–1942 related to El Nino,
1084 *Nature*, 431, 971–974, 2004.

1085

1086 Brunner, D., Staehelin, J., Maeder, J. A., Wohltmann, I., and Bodeker, G. E.: Variability and
1087 trends in total and vertically resolved stratospheric ozone based on the CATO ozone data set,
1088 *Atmos. Chem. Phys.*, 6, 4985–5008, doi:10.5194/acp-6-4985-2006, 2006.

1089

1090 Buffet, L., Villaret, C., Jacquette, E., Vandermarcq, O., Astruc, P., and Anstötz, S.: Status of
1091 IASI instruments onboard Metop-A and Metop-B satellites, 4th IASI International Conference,
1092 Antibes Juan-Les-Pins, France, 11–15 April 2016, available at:
1093 [https://iasi.cnes.fr/sites/default/files/drupal/201612/default/bpc_iasi-conference4-](https://iasi.cnes.fr/sites/default/files/drupal/201612/default/bpc_iasi-conference4-1_02_instruments_buffet.pdf)
1094 [1_02_instruments_buffet.pdf](https://iasi.cnes.fr/sites/default/files/drupal/201612/default/bpc_iasi-conference4-1_02_instruments_buffet.pdf) (last access: 30 August 2018), 2016.

1095

1096 Butler, A. H., M. Polvani, and C. Deser: Separating the stratospheric and tropospheric pathways
1097 of El Niño–Southern Oscillation teleconnections, *Environ. Res. Lett.*, 9, 2, 024014,
1098 doi:10.1088/1748-9326/9/2/024014, 2014.

1099

1100 Cagnazzo, C., E. Manzini, N. Calvo, A. Douglass, H. Akiyoshi, S. Bekki, M. Chipperfield, M.
1101 Dameris, M. Deushi, A. M. Fischer, H. Garny, A. Gettelman, M. A. Giorgetta, D. Plummer, E.
1102 Rozanov, T. G. Shepherd, K. Shibata, A. Stenke, H. Struthers and W. Tian: Northern winter
1103 stratospheric temperature and ozone responses to ENSO inferred from an ensemble of Chemistry
1104 Climate Models, *Atmos. Chem. Phys.*, 9, 8935–8948, www.atmos-chem-phys.net/9/8935/2009/,
1105 2009.

1106

1107 Chabrillat, S., Vigouroux, C., Christophe, Y., Engel, A., Errera, Q., Minganti, D., Monge-Sanz,
1108 B. M., Segers, A., and Mahieu, E.: Comparison of mean age of air in five reanalyses using the
1109 BASCOE transport model, *Atmos. Chem. Phys.*, 18, 14715–14735, 2018.

1110

1111 Chipperfield, M. P., Kinnersley, J. S., and Zawodny, J.: A twodimensional model study of the
1112 QBO signal in SAGE II NO₂ and O₃, *Geophys. Res. Lett.*, 21, 589–592, 1994.

1113

1114 Chubachi, S.: Preliminary results of ozone observations at Syowa Station from February 1982 to
1115 January 1983, in: *Proc. Sixth Symposium on Polar Meteorology and Glaciology*, edited by:
1116 Kusunoki, K., vol. 34 of *Mem. National Institute of Polar Research Special Issue*, 13–19, 1984.

1117

1118 Clarisse, L., Clerbaux, C., Franco, B., Hadji-Lazaro, J., Whitburn, S., Kopp, A. K., D. Hurtmans
1119 and P.-F. Coheur: A decadal data set of global atmospheric dust retrieved from IASI satellite
1120 measurements, *J. Geophys. Res.*, 124, <https://doi.org/10.1029/2018JD029701>, 2019.

1121

1122 Coldewey-Egbers, M., D. G. Loyola R., P. Braesicke, M. Dameris, M. van Roozendaal, C. Lerot,
1123 and W. Zimmer: A new health check of the ozone layer at global and regional scales, *Geophys.*
1124 *Res. Lett.*, 41, 4363–4372, doi:10.1002/2014GL060212, 2014.

1125

1126 Clerbaux, C., A. Boynard, L. Clarisse, M. George, J. Hadji-Lazaro, H. Herbin, D. Hurtmans, M.
1127 Pommier, A. Razavi, S. Turquety, C. Wespes, and P.-F. Coheur: Monitoring of atmospheric
1128 composition using the thermal infrared IASI/MetOp sounder, *Atmos. Chem. Phys.*, 9, 6041–
1129 6054, 2009.

1130

1131 Clerbaux, C. and Crevoisier, C.: New Directions: Infrared remote sensing of the troposphere
1132 from satellite: Less, but better, *Atmos. Environ.*, 72, 24–26, 2013.

1133

1134 Cochran, D. and Orcutt, G. H.: Application of least squares regression to relationships
1135 containing auto-correlated error terms, *J. Am. Stat. Assoc.*, 44, 32–61, 1949.

1136

1137 Crevoisier, C., Clerbaux, C., Guidard, V., Phulpin, T., Armante, R., Barret, B., Camy-Peyret, C.,
1138 Chaboureaud, J.-P., Coheur, P.-F., Crépeau, L., Dufour, G., Labonnote, L., Lavanant, L., Hadji-
1139 Lazaro, J., Herbin, H., Jacquinet-Husson, N., Payan, S., Péquignot, E., Pierangelo, C., Sellitto,
1140 P., and Stubenrauch, C.: Towards IASI-New Generation (IASI-NG): impact of improved

1141 spectral resolution and radiometric noise on the retrieval of thermodynamic, chemistry and
1142 climate variables, *Atmos. Meas. Tech.*, 7, 4367–4385, 2014.

1143

1144 Crutzen, P. J.: Estimates of possible future ozone reductions from continued use of fluoro-
1145 chloro-methanes (CF₂Cl₂, CFC13), *Geophys. Res. Lett.*, 1, 205–208,
1146 <https://doi.org/10.1029/GL001i005p00205>, 1974.

1147

1148 Dhomse, S., Weber, M., Wohltmann, I., Rex, M., and Burrows, J. P.: On the possible causes of
1149 recent increases in northern hemispheric total ozone from a statistical analysis of satellite data
1150 from 1979 to 2003, *Atm. Chem. Phys.*, 6, 1165–1180, 2006.

1151

1152 Dhomse, S. S., Chipperfield, P., Feng, W., Hossaini, R., Mann G. W., and Santee, M. L.:
1153 Revisiting the hemispheric asymmetry in midlatitude ozone changes following the Mount
1154 Pinatubo eruption: A 3-D model study, *Geophys. Res. Lett.*, 42, 3038–3047, 2015.

1155

1156 Domeisen, D. I., Garfinkel, C. I., and Butler, A. H.: The teleconnection of El Niño Southern
1157 Oscillation to the stratosphere, *Reviews of Geophysics*, 57,
1158 <https://doi.org/10.1029/2018RG000596>, 2019.

1159

1160 Errera, Q., S. Chabrillat, Y. Christophe, J. Debossher, D. Hubert, W. Lahoz, M. Santee, M.
1161 Shiotani, S. Skachko, T. von Clarmann, and K. Walker: Reanalysis of Aura MLS Chemical
1162 Observations submitted to *Atms. Chem. Phys. Discuss.*, doi:10.5194/acp-2019-530, 2019.

1163

1164 Farman, J. C., Gardiner, B. G., and Shanklin, J. D.: Large losses of total ozone in Antarctica
1165 reveal seasonal ClO_x/NO_x interaction, *Nature*, 315, 207–210, doi:10.1038/315207a0, 1985.

1166

1167 Farmer, C. B., G. C. Toon, P. W. Shaper, J. F. Blavier, and L. L. Lowes, Stratospheric trace
1168 gases in the spring 1986 Antarctic atmosphere, *Nature*, 329, 126–130, 1987.

1169

1170 Fioletov, V. E. and Shepherd, T. G.: Seasonal persistence of midlatitude total ozone anomalies,
1171 *Geophys. Res. Lett.*, 30, 1417, doi:10.1029/2002GL016739, 2003.

1172

1173 Fioletov, V. E. and Shepherd, T. G.: Summertime total ozone variations over middle and polar
1174 latitudes, *Geophys. Res. Lett.*, 32, 4807, doi:10.1029/2004GL022080, 2005.

1175

1176 Fishman, J., J.K. Creilson, A.E. Wozniak, and P.J. Crutzen, The interannual variability of
1177 stratospheric and tropospheric ozone determined from satellite measurements, *J. Geophys. Res.*,
1178 110, D20306, doi:10.1029/2005JD005868, 2005.

1179

1180 Frossard, L., H.E. Rieder, M. Ribatet, J. Staehelin, J. A. Maeder, S. Di Rocco, A. C. Davison, T.
1181 Pete.: On the relationship between total ozone and atmospheric dynamics and chemistry at mid-
1182 latitudes – Part 1: Statistical models and spatial fingerprints of atmospheric dynamics and
1183 chemistry, *Atmos. Chem. Phys.*, 13, 147–164, doi:10.5194/acp-13-147-2013, 2013.

1184

1185 Fusco, A. C. and Salby, M. L.: Interannual variations of total ozone and their relationship to
1186 variations of planetary wave activity, *J. Clim.*, 12, 1619–1629, 1999.
1187

1188 Galytzka, E., Rozanov, A., Chipperfield, M. P., Dhomse, Sandip. S., Weber, M., Arosio, C.,
1189 Feng, W., and Burrows, J. P.: Dynamically controlled ozone decline in the tropical mid-
1190 stratosphere observed by SCIAMACHY, *Atmos. Chem. Phys.*, 19, 767-783,
1191 <https://doi.org/10.5194/acp-19-767-2019>, 2019.
1192

1193 Gebhardt, C., Rozanov, A., Hommel, R., Weber, M., Bovensmann, H., Burrows, J. P.,
1194 Degenstein, D., Froidevaux, L., and Thompson, A. M.: Stratospheric ozone trends and variability
1195 as seen by SCIAMACHY from 2002 to 2012, *Atmos. chem. Phys.*, 14, 831–846,
1196 <https://doi.org/10.5194/acp-14-831-2014>, 2014.
1197

1198 Harris, N. R. P., Hassler, B., Tummon, F., Bodeker, G. E., Hubert, D., Petropavlovskikh, I.,
1199 Steinbrecht, W., Anderson, J., Bhartia, P. K., Boone, C. D., Bourassa, A., Davis, S. M.,
1200 Degenstein, D., Delcloo, A., Frith, S. M., Froidevaux, L., Godin-Beekmann, S., Jones, N.,
1201 Kurylo, M. J., Kyrölä, E., Laine, M., Leblanc, S. T., Lambert, J.-C., Liley, B., Mahieu, E.,
1202 Maycock, A., De Mazière, M., Parrish, A., Querel, R., Rosenlof, K. H., Roth, C., Sioris, C.,
1203 Staehelin, J., Stolarski, R. S., Stübi, R., Tamminen, J., Vigouroux, C., Walker, K. A., Wang, H.
1204 J., Wild, J., and Zawodny, J. M.: Past changes in the vertical distribution of ozone – Part 3:
1205 Analysis and interpretation of trends, *Atmos. Chem. Phys.*, 15, 9965-9982,
1206 <https://doi.org/10.5194/acp-15-9965-2015>, 2015.
1207

1208 Harrison, D. E., and Larkin, N. K.: El Niño-Southern Oscillation sea surface temperature and
1209 wind anomalies, 1946–1993, *Rev. Geophys.*, 36, 353–399, doi:10.1029/98RG00715, 1998.
1210

1211 Hilton, F., R. Armante, T. August, et al. : Hyperspectral Earth Observation from IASI: Five
1212 Years of Accomplishments, *Bulletin of the American Meteorological Society*, vol. 93, issue 3,
1213 pp. 347-370, 2012.
1214

1215 Hofmann, D. J. and Solomon, S.: Ozone destruction through heterogeneous chemistry following
1216 the eruption of El Chichón, *J. Geophys. Res.*, 94, 5029,
1217 <https://doi.org/10.1029/JD094iD04p05029>, 1989.
1218

1219 Hofmann, D. J., S. J. Oltmans, Antarctic ozone during 1992: Evidence for Pinatubo volcanic
1220 aerosol effects. *J. Geophys. Res.* 98, 18555–18561, doi:10.1029/93JD02092, 1993.
1221

1222 Hofmann, D. J., S. J. Oltmans, J. M. Harris, B. J. Johnson, and J. A. Lathrop: Ten years of
1223 ozonesonde measurements at the south pole: Implications for recovery of springtime Antarctic
1224 ozone, *J. Geophys. Res.*, 102(D7), 8931– 8943, doi:10.1029/96JD03749, 1997.
1225

1226 Hood, L. L., McCormick, J. P., and Labitzke, K.: An investigation of dynamical contributions to
1227 midlatitude ozone trends in winter, *J. Geophys. Res.*, 102, 13 079–13 093, 1997.
1228

1229 Hood, L. L., and B. E. Soukharev: Quasi-decadal variability of the tropical lower stratosphere:
1230 The role of extratropical wave forcing, *J. Atmos. Sci.*, 60, 2389–2403, 2003.
1231

1232 Hood, L. L., and B. E. Soukharev: Solar induced variations of odd nitrogen: Multiple regression
1233 analysis of UARS HALOE data, *Geophys. Res. Lett.*, doi:10.1029/2006GL028122, 2006.
1234

1235 Hubert, D., Lambert, J.-C., Verhoelst, T., Granville, J., Keppens, A., Baray, J.-L., Bourassa, A.
1236 E., Cortesi, U., Degenstein, D. A., Froidevaux, L., Godin-Beekmann, S., Hoppel, K. W.,
1237 Johnson, B. J., Kyrölä, E., Leblanc, T., Lichtenberg, G., Marchand, M., McElroy, C. T.,
1238 Murtagh, D., Nakane, H., Portafaix, T., Querel, R., Russell III, J. M., Salvador, J., Smit, H. G. J.,
1239 Stebel, K., Steinbrecht, W., Strawbridge, K. B., Stübi, R., Swart, D. P. J., Taha, G., Tarasick, D.
1240 W., Thompson, A. M., Urban, J., van Gijsel, J. A. E., Van Malderen, R., von der Gathen, P.,
1241 Walker, K. A., Wolfram, E., and Zawodny, J. M.: Ground-based assessment of the bias and long-
1242 term stability of 14 limb and occultation ozone profile data records, *Atmos. Meas. Tech.*, 9,
1243 2497-2534, <https://doi.org/10.5194/amt-9-2497-2016>, 2016.
1244

1245 Hurrell, J. W.: Decadal trends in the North Atlantic Oscillation regional temperatures and
1246 precipitation, *Science*, 269, 676–679, 1995.
1247

1248 Hurtmans, D., P. Coheur, C. Wespes, L. Clarisse, O. Scharf, C. Clerbaux, J. Hadji-Lazaro, M.
1249 George, and S. Turquety: FORLI radiative transfer and retrieval code for IASI, *Journal of*
1250 *Quantitative Spectroscopy and Radiative Transfer*, 113, 1391-1408, 2012.
1251

1252 Jackman, C., E. Fleming, and F. Vitt: Influence of extremely large solar proton events in a
1253 changing stratosphere, *J. Geophys. Res.*, 105, 11 659–11 670, 2000.
1254

1255 Jonsson, A. I., de Grandpré, J., Fomichev, V. I., McConnell, J. C., and Beagley, S. R.: Doubled
1256 CO₂-induced cooling in the middle atmosphere: photochemical analysis of the ozone radiative
1257 feedback, *J. Geophys. Res.*, 109, D24103, <https://doi.org/10.1029/2004JD005093>, 2004.
1258

1259 Kalnay, E., M. Kanamitsu, R. Kistler, W. Collins, D. Deaven, L. Gandin, M. Iredell, S. Saha, G.
1260 White, J. Woollen, Y. Zhu, M. Chelliah, W. Ebisuzaki, W. Higgins, J. Janowiak, K.C. Mo, C.
1261 Ropelewski, J. Wang, A. Leetmaa, R. Reynolds, R. Jenne, and D. Joseph, 1996: The
1262 NCEP/NCAR 40-Year Reanalysis Project. *Bull. Amer. Meteor. Soc.*, 77, 437–472,
1263 <https://doi.org/10.1175/1520-0477>, 1996.
1264

1265 Keeble, J., Brown, H., Abraham, N. L., Harris, N. R. P., and Pyle, J. A.: On ozone trend
1266 detection: using coupled chemistry–climate simulations to investigate early signs of total column
1267 ozone recovery, *Atmos. Chem. Phys.*, 18, 7625-7637, <https://doi.org/10.5194/acp-18-7625-2018>,
1268 2018.
1269

1270 Keppens, A., J.-C. Lambert, J. Granville, D. Hubert, T. Verhoelst, S. Compernelle, B. Latter, B.
1271 Kerridge, R. Siddans, A. Boynard, J. Hadji-Lazaro, C. Clerbaux, C. Wespes, D. R. Hurtmans, P.-
1272 F. Coheur, J. van Peet, R. van der A, K. Garane, M. E. Koukouli, D. S. Balis, A. Delcloo, R.
1273 Kivi, R. Stübi, S. Godin-Beekmann, M. Van Roozendaal, C. Zehner: Quality assessment of the

1274 Ozone_cci Climate Research Data Package (release 2017): 2. Ground-based validation of nadir
1275 ozone profile data products, in preparation for this QOS special issue.
1276

1277 Kyrölä, E., Laine, M., Sofieva, V., Tamminen, J., Päivärinta, S.-M., Tukiainen, S., Zawodny, J.,
1278 and Thomason, L.: Combined SAGE II-GOMOS ozone profile data set for 1984–2011 and trend
1279 analysis of the vertical distribution of ozone, *Atmos. Chem. Phys.*, 13, 10645–10658,
1280 <https://doi.org/10.5194/acp-13-10645-2013>, 2013.
1281

1282 Kodera, K. and Kuroda, Y.: Dynamical response to the solar cycle: Winter stratopause and lower
1283 stratosphere, *J. Geophys. Res.*, 107, 4749, doi:10.1029/2002JD002224, 2002.
1284

1285 Kuttippurath, J., F. Lefèvre, J.-P. Pommereau, H. K. Roscoe, F. Goutail, A. Pazmiño, J. D.
1286 Shanklin, Antarctic ozone loss in 1979–2010: First sign of ozone recovery. *Atmos. Chem. Phys.*
1287 13, 1625–1635, doi:10.5194/acp-13-1625-2013, 2013.
1288

1289 Kuttippurath, J., and P.J. Nair: The signs of Antarctic ozone hole recovery 2017, *Scientific*
1290 *Reports*, 7, 585, doi:10.1038/s41598-017-00722-7, 2017.
1291

1292 Labitzke, K. and van Loon, H.: The QBO effect on the solar signal in the global stratosphere in
1293 the winter of the Northern Hemisphere, *J. Atmos. Solar-Terr. Phys.*, 62, 621–628, 2000.
1294

1295 Mäder, J. A., J. Staehelin, D. Brunner, W.A. Stahel, I. Wohltmann, and T. Peter: Statistical
1296 modelling of total ozone: Selection of appropriate explanatory variables, *J. Geophys. Res.*, 112,
1297 D11108, doi:10.1029/2006JD007694, 2007.
1298

1299 Mäder, J. A., J. Staehelin, T. Peter, D. Brunner, H. E. Rieder, and W. A. Stahel: Evidence for the
1300 effectiveness of the Montreal Protocol to protect the ozone layer, *Atmos. Chem. Phys.*, 10, 24,
1301 12,161–12,171, doi:10.5194/acp-10-12161-2010, 2010.

1302 Manatsa, D. and G. Mukwada: A connection from stratospheric ozone to El Niño-Southern
1303 Oscillation, *Scientific Reports*, 7, 5558, DOI:10.1038/s41598-017-05111-8, 2017.

1304 Manzini, E., Giorgetta, M. A., Esch, M., Kornblueh, L., and Roeckner, E.: The influence of sea
1305 surface temperatures on the northern winter stratosphere: Ensemble simulations with the
1306 MAECHAM5 model, *J. Climate*, 19, 3863–3881, 2006.
1307

1308 McCormack, J. P., D. E. Siskind, and L. L. Hood: Solar-QBO interaction and its impact on
1309 stratospheric ozone in a zonally averaged photochemical transport model of the middle
1310 atmosphere, *J. Geophys. Res.*, 112, D16109, doi:10.1029/2006JD008369, 2007.
1311

1312 McPeters, R. D., G.J. Labow, and J.A. Logan: Ozone climatological profiles for satellite retrieval
1313 algorithms, *J. Geophys. Res.-Atmos.*, 112, D05308, doi:10.1029/2005JD006823, 2007.
1314

1315 Molina, M. J. and Rowland, F. S.: Stratospheric sink for chlorofluoromethanes: Chlorine atom-
1316 catalysed destruction of ozone, *Nature*, 249, 810–812, 1974.

1317
1318 Nair, P. J., Froidevaux, L., Kuttippurath, J., Zawodny, J. M., Russell, J. M., Steinbrecht, W.,
1319 Claude, H., Leblanc, T., van Gijssel, J. A. E., Johnson, B., Swart, D. P. J., Thomas, A., Querel, R.,
1320 Wang, R., and Anderson, J.: Subtropical and midlatitude ozone trends in the stratosphere:
1321 Implications for recovery, *J. Geophys. Res.-Atmos.*, 120, 7247–7257,
1322 <https://doi.org/10.1002/2014JD022371>, 2015.

1323
1324 Newchurch, M. J., Yang, E.-S., Cunnold, D. M., Reinsel, G. C., Zawodny, J. M., and Russell III,
1325 J. M.: Evidence for slowdown in stratospheric ozone loss: First stage of ozone recovery, *J.*
1326 *Geophys. Res.*, 108, 4507, doi:10.1029/2003JD003471, 2003.

1327
1328 Newman, P. A., Nash, E. R., Kawa, S. R., Montzka, S. A., and Schauffler, S. M.: When will the
1329 Antarctic ozone hole recover?: *Geophys. Res. Lett.*, 33, L12814, doi:10.1029/2005GL025232,
1330 2006.

1331
1332 Oman, L. D., Douglass, A. R., Ziemke, J. R., Rodriguez, J. M., Waugh, D. W., and Nielsen, J.
1333 E.: The ozone response to ENSO in Aura satellite measurements and a chemistry–climate
1334 simulation, *J. Geophys. Res.-Atmos.*, 118, 965–976, 2013.

1335
1336 Pawson, S., Steinbrecht, W., Charlton-Perez, A J Fujiwara, M., Karpechko, A. Y.,
1337 Petropavlovskikh, I., Urban, J., and Weber, M.: Update on Global Ozone: Past, Present, and
1338 Future, in: *Scientific Assessment of Ozone Depletion: 2014*, World Meteorological
1339 Organization, Global Ozone Research and Monitoring Project – Report No. 55, chap. 2, World
1340 Meteorological Organization/UNEP, 2014.

1341
1342 Portmann, R. W., S. Solomon, R. R. Garcia, L. W. Thomason, L. R. Poole, M. P. McCormick,
1343 Role of aerosol variations in anthropogenic ozone depletion in the polar regions. *J. Geophys.*
1344 *Res.* 101, 22991–23006, doi:10.1029/96JD02608, 1996.

1345
1346 Knudsen, B. M. and Grooss, J.: Northern midlatitude stratospheric ozone dilution in spring
1347 modeled with simulated mixing, *J. Geophys. Res.*, 105, 6885–6890, 2000.

1348
1349 Randel, W. J. and Cobb, J. B.: Coherent variations of monthly mean total ozone and lower
1350 stratospheric temperature, *J. Geophys. Res.-Atmos.*, 99, 5433–5447, 1994.

1351
1352 Randel, W. J. and F. Wu: Isolation of the ozone QBO in SAGE II data by singular-value
1353 decomposition, *J. Atmos. Sci.*, 53, 2546– 2559, 1996.

1354
1355 Randel, W. J., F. Wu, and R. Stolarski: Changes in column ozone correlated with the
1356 stratospheric EP flux, *J. Meteorol. Soc. Jpn.*, 80, 849–862, 2002.

1357
1358 Randel, W. J., Garcia, R. R., Calvo, N., and Marsh, D.: ENSO influence on zonal mean
1359 temperature and ozone in the tropical lower stratosphere, *Geophys. Res. Lett.*, 36, L15822,
1360 <https://doi.org/10.1029/2009GL039343>, 2009.

1361

1362 Randel, W. J., and A. M. Thompson: Interannual variability and trends in tropical ozone derived
1363 from SAGE II satellite data and SHADOZ ozonesondes, *J. Geophys. Res.*, 116, D07303,
1364 doi:10.1029/2010JD015195, 2011.
1365
1366 Reinsel, G. C., Miller, A. J., Weatherhead, E. C., Flynn, L. E., Nagatani, R. M., Tiao, G. C., and
1367 Wuebbles, D. J.: Trend analysis of total ozone data for turnaround and dynamical contributions,
1368 *J. Geophys. Res.*, 110, D16306, doi:10.1029/2004JD004662, 2005.
1369
1370 Revell, L. E., Stenke, A., Luo, B., Kremser, S., Rozanov, E., Sukhodolov, T., and Peter, T.:
1371 Impacts of Mt Pinatubo volcanic aerosol on the tropical stratosphere in chemistry–climate model
1372 simulations using CCM1 and CMIP6 stratospheric aerosol data, *Atmos. Chem. Phys.*, 17, 13139–
1373 13150, 2017.
1374
1375 Rex, M., Salawitch, R. J., von der Gathen, P., Harris, N. R. P., Chipperfield, M. P., and
1376 Naujokat, B.: Arctic ozone loss and climate change, *Geophys. Res. Lett.*, 32, L04116,
1377 doi:10.1029/2003GL018844, 2004.
1378
1379 Rieder, H. E., Frossard, L., Ribatet, M., Staehelin, J., Maeder, J. A., Di Rocco, S., Davison, A.
1380 C., Peter, T., Weihs, P., and Holawe, F.: On the relationship between total ozone and atmospheric
1381 dynamics and chemistry at mid-latitudes – Part 2: The effects of the El Niño/Southern
1382 Oscillation, volcanic eruptions and contributions of atmospheric dynamics and chemistry to
1383 long-term total ozone changes, *Atmos. Chem. Phys.*, 13, 165–179, 2013.
1384
1385 Rind, D., Perlwitz, J., and Lonergan, P.: AO/NAO response to climate change: 1. Respective
1386 influences of stratospheric and tropospheric climate changes, *J. Geophys. Res.*, 110, D12107,
1387 doi: 10.1029/2004JD005103, 2005.
1388
1389 Rodgers, C. D.: *Inverse Methods for Atmospheric Sounding: Theory and Practice*, World
1390 Scientific, Series on Atmospheric, Oceanic and Planetary Physics, 2, Hackensack, N. J., 2000.
1391
1392 Salby, M., E. Titova, and L. Deschamps: Rebound of Antarctic ozone, *Geophys. Res. Lett.*, 38,
1393 L09702, doi:10.1029/2011GL047266, 2011.
1394
1395 Schnadt, C. and Dameris, M.: Relationship between North Atlantic Oscillation changes and
1396 stratospheric ozone recovery in the Northern Hemisphere in a chemistry-climate model, *J.*
1397 *Geophys. Res.*, 30, 1487, doi:10.1029/2003GL017006, 2003.
1398
1399 Shepherd, T. G., Plummer, D. A., Scinocca, J. F., Hegglin, M. I., Fioletov, V. E., Reader, M. C.,
1400 Remsberg, E., von Clarmann, T., and Wang, H. J.: Reconciliation of halogen-induced ozone loss
1401 with the total-column ozone record, *Nat. Geosci.*, 7, 443–449, <https://doi.org/10.1038/ngeo2155>,
1402 2014.
1403
1404 Sioris, C. E., McLinden, C. A., Fioletov, V. E., Adams, C., Zawodny, J. M., Bourassa, A. E.,
1405 Roth, C. Z., and Degenstein, D. A.: Trend and variability in ozone in the tropical lower

1406 stratosphere over 2.5 solar cycles observed by SAGE II and OSIRIS, *Atmos. Chem. Phys.*, 14,
1407 3479–3496, <https://doi.org/10.5194/acp-14-3479-2014>, 2014.
1408
1409 Sofieva, V. F., Kyrölä, E., Laine, M., Tamminen, J., Degenstein, D., Bourassa, A., Roth, C.,
1410 Zawada, D., Weber, M., Rozanov, A., Rahpoe, N., Stiller, G., Laeng, A., von Clarmann, T.,
1411 Walker, K. A., Sheese, P., Hubert, D., van Roozendaal, M., Zehner, C., Damadeo, R., Zawodny,
1412 J., Kramarova, N., and Bhartia, P. K.: Merged SAGE II, Ozone_cci and OMPS ozone profile
1413 dataset and evaluation of ozone trends in the stratosphere, *Atmos. Chem. Phys.*, 17, 12533–
1414 12552, <https://doi.org/10.5194/acp-17-12533-2017>, 2017.
1415
1416 Solomon, S., R. R. Garcia, F. S. Rowland, and D. J. Wuebbles, On the depletion of Antarctic
1417 zone, *Nature*, 321, 755–758, 1986.
1418
1419 Solomon, S., Portman, R. W., Garcia, R. R., Thomason, L. W., Poole, L. R., and McCormack,
1420 M. P.: The role of aerosol variations in anthropogenic ozone depletion at northern midlatitudes,
1421 *J. Geophys. Res.*, 101, 6713–6727, 1996.
1422
1423 Solomon, S.: Stratospheric ozone depletion: A review of concepts and history. *Rev. Geophys.*
1424 37, 275–316, doi:10.1029/1999RG900008, 1999.
1425
1426 Solomon, P., Barrett, J., Mooney, T., Connor, B., Parrish, A., and Siskind, D. E.: Rise and
1427 decline of active chlorine in the stratosphere, *Geophys. Res. Lett.*, 33, L18807,
1428 <https://doi.org/10.1029/2006GL027029>, 2006.
1429
1430 Solomon, S., Ivy, D. J., Kinnison, D., Mills, M. J., Neely, R. R., and Schmidt, A.: Emergence of
1431 healing in the Antarctic ozone layer, *Science*, 353, 269–274,
1432 <https://doi.org/10.1126/science.aae0061>, 2016.
1433
1434 Stolarski, R. S., A. J. Krueger, M. R. Schoeberl, R. D. Mc-Peters, P. A. Newman, and J. C.
1435 Alpert, Nimbus 7 satellite measurements of the springtime Antarctic ozone decrease, *Nature*,
1436 322, 808–811, 1986.
1437
1438 Soukharev, B. E. and L. L. Hood: Solar cycle variation of stratospheric ozone: Multiple
1439 regression analysis of long-term satellite data sets and comparisons with models, *J. Geophys.*
1440 *Res.*, 111, D20314, doi:10.1029/2006JD007107, 2006.
1441
1442 Steinbrecht, W., H. Claude, U. Köhler, and K. P. Hoinka: Correlations between tropopause
1443 height and total ozone: Implications for long-term changes, *J. Geophys. Res.*, 103, 19,183–
1444 19,192, doi:10.1029/98JD01929, 1998.
1445
1446 Steinbrecht, W., B. Hassler, H. Claude, P. Winkler, and R. S. Stolarski: Global distribution of
1447 total ozone and lower stratospheric temperature variations, *Atmos. Chem. Phys.*, 3, 1421–1438,
1448 2003.
1449

1450 Steinbrecht, W., et al.: Interannual variation patterns of total ozone and lower stratospheric
1451 temperature in observations and model simulations, *Atmos. Chem. Phys.*, 6, 349–374,
1452 doi:10.5194/acp-6-349-2006, 2006
1453
1454 Steinbrecht, W., Froidevaux, L., Fuller, R., Wang, R., Anderson, J., Roth, C., Bourassa, A.,
1455 Degenstein, D., Damadeo, R., Zawodny, J., Frith, S., McPeters, R., Bhartia, P., Wild, J., Long,
1456 C., Davis, S., Rosenlof, K., Sofieva, V., Walker, K., Ralpoe, N., Rozanov, A., Weber, M.,
1457 Laeng, A., von Clarmann, T., Stiller, G., Kramarova, N., Godin-Beekmann, S., Leblanc, T.,
1458 Querel, R., Swart, D., Boyd, I., Hocke, K., Kämpfer, N., Maillard Barras, E., Moreira, L.,
1459 Nedoluha, G., Vigouroux, C., Blumenstock, T., Schneider, M., García, O., Jones, N., Mahieu, E.,
1460 Smale, D., Kotkamp, M., Robinson, J., Petropavlovskikh, I., Harris, N., Hassler, B., Hubert, D.,
1461 and Tummon, F.: An update on ozone profile trends for the period 2000 to 2016, *Atmos. Chem.*
1462 *Phys.*, 17, 10675–10690, doi:10.5194/acp-17-10675-2017, 2017.
1463
1464 Thomason, L. W., Ernest, N., Millán, L., Rieger, L., Bourassa, A., Vernier, J.-P., Manney, G.,
1465 Luo, B., Arfeuille, F., and Peter, T.: A global space-based stratospheric aerosol climatology:
1466 1979–2016, *Earth Syst. Sci. Data*, 10, 469-492, <https://doi.org/10.5194/essd-10-469-2018>, 2018.
1467
1468 Thompson, D. W. J. and J.M. Wallace: Annular modes in the extratropical circulation. Part I:
1469 month-to-month variability, *J. Climate*, 13, 1000–1016, 2000.
1470
1471 Thompson, D. W. J. and Solomon, S.: Interpretation of Recent Southern Hemisphere Climate
1472 Change, *Science*, 296, 895-899, 2002.
1473
1474 Tian, W., M.P. Chipperfield, L.J. Gray, and J.M. Zawodny: Quasi-biennial oscillation and tracer
1475 distributions in a coupled chemistry-climate model, *J. Geophys. Res.*, 111, D20301,
1476 doi:10.1029/2005JD006871, 2006.
1477
1478 Tiao, G. C., G. C. Reinsel, D. Xu, J. H. Pedrick, X. Zhu, A. J. Miller, J. J. DeLuisi, C. L. Mateer,
1479 and D. J. Wuebbles, Effects of autocorrelation and temporal sampling schemes on estimates of
1480 trend and spatial correlation, *J. Geophys Res.*, 95, 20,507-20,517, 1990.
1481
1482 Tweedy, O. V., Waugh, D. W., Randel, W. J., Abalos, M., Oman, L. D. and Kinnison, D. E.: The
1483 impact of boreal summer ENSO events on tropical lower stratospheric ozone, *J. Geophys. Res.*,
1484 *Atmospheres*, 123, 9843–9857, doi:10.1029/2018JD029020, 2018.
1485
1486 Valks, P., N. Hao, S. Gimeno Garcia, D. Loyola, M. Dameris, P. Jöckel, and A. Delcloo:
1487 Tropical tropospheric ozone column retrieval for GOME-2, *Atmos. Meas. Tech.*, 7, 2513–2530,
1488 doi:10.5194/amt-7-2513-2014, 2014.
1489
1490 Vigouroux, C., Blumenstock, T., Coffey, M., Errera, Q., García, O., Jones, N. B., Hannigan, J.
1491 W., Hase, F., Liley, B., Mahieu, E., Mellqvist, J., Notholt, J., Palm, M., Persson, G., Schneider,
1492 M., Servais, C., Smale, D., Thölix, L., and De Mazière, M.: Trends of ozone total columns and
1493 vertical distribution from FTIR observations at eight NDACC stations around the globe, *Atmos.*
1494 *Chem. Phys.*, 15, 2915–2933, <https://doi.org/10.5194/acp-15-2915-2015>, 2015.

1495
1496 Weatherhead, E.C., G. C. Reinsel, G. C. Tiao, X.-L. Meng, D. Choi, W.-K. Cheang, T. Keller, J.
1497 DeLuisi, D. J. Wuebbles, J. B. Kerr, A. J. Miller, S. J. Oltmans and J. E. Frederick: Factors
1498 affecting the detection of trends: Statistical considerations and applications to environmental
1499 data, *J. Geophys. Res. Atmos.*, 103, 17149–17161, 1998.
1500
1501 Weber, M., Dikty, S., Burrows, J. P., Garny, H., Dameris, M., Kubin, A., Abalichin, J., and
1502 Langematz, U.: The Brewer-Dobson circulation and total ozone from seasonal to decadal time
1503 scales, *Atmos. Chem. Phys.*, 11, 11221-11235, <https://doi.org/10.5194/acp-11-11221-2011>,
1504 2011.
1505
1506 Weber, M., Coldewey-Egbers, M., Fioletov, V. E., Frith, S. M., Wild, J. D., Burrows, J. P.,
1507 Long, C. S., and Loyola, D.: Total ozone trends from 1979 to 2016 derived from five merged
1508 observational datasets – the emergence into ozone recovery, *Atmos. Chem. Phys.*, 18, 2097–
1509 2117, <https://doi.org/10.5194/acp-18-2097-2018>, 2018.
1510
1511 Wespes, C., D. Hurtmans, L.K. Emmons, S. Safieddine, C. Clerbaux, D.P. Edwards, and P.-F.
1512 Coheur: Ozone variability in the troposphere and the stratosphere from the first six years of IASI
1513 observations (2008-2013), *Atmos. Chem. Phys.*, 16, 5721-5743, 2016.
1514
1515 Wespes, C., D. Hurtmans, C. Clerbaux, and P.-F. Coheur: O₃ variability in the troposphere as
1516 observed by IASI over 2008–2016 — Contribution of atmospheric chemistry and dynamics, *J.*
1517 *Geophys. Res. Atmos.*, 122, 2429–2451, doi:10.1002/2016JD025875, 2017.
1518
1519 Wespes, C., Hurtmans, D., Clerbaux, C., Boynard, A., and Coheur, P.-F.: Decrease in
1520 tropospheric O₃ levels in the Northern Hemisphere observed by IASI, *Atmos. Chem. Phys.*, 18,
1521 6867–6885, <https://doi.org/10.5194/acp-18-6867-2018>, 2018.
1522
1523 Witte, J. C., M.R. Schoeberl, A.R. Douglass, and A.M. Thompson: The Quasi-biennial
1524 Oscillation and annual variations in tropical ozone from SHADOZ and HALOE, *Atmos. Chem.*
1525 *Phys.*, 8, 3929–3936, 2008.
1526
1527 World Meteorological Organization (WMO): Scientific Assessment of Ozone Depletion: 2006,
1528 Global Ozone Research and Monitoring Project, Report No. 50, Geneva, Switzerland, 2007.
1529
1530 World Meteorological Organization (WMO): Scientific Assessment of Ozone Depletion: 2010,
1531 Global Ozone Research and Monitoring Project, Report No. 52, Geneva, Switzerland, 2011.
1532
1533 World Meteorological Organization (WMO): Scientific Assessment of Ozone Depletion: 2014,
1534 Global Ozone Research and Monitoring Project, Report No. 55, Geneva, Switzerland, 2014.
1535
1536 World Meteorological Organization (WMO): Scientific Assessment of Ozone Depletion: 2018,
1537 Global Ozone Research and Monitoring Project, Report No. 58, Geneva, Switzerland, 2018.
1538

- 1539 Wohltmann, I., R. Lehmann, M. Rex, D. Brunner, and J. A. Maeder: A process-oriented
1540 regression model for column ozone, *J. Geophys. Res.*, *112*, D12304, doi:10.1029/2006JD007573,
1541 2007.
- 1542
- 1543 Yang, E.-S., D. M. Cunnold, M. J. Newchurch, R. J. Salawitch, M. P. McCormick, J. M. Russell
1544 III, J. M. Zawodny, S. J. Oltmans: First stage of Antarctic ozone recovery. *J. Geophys. Res.* *113*,
1545 D20308, doi:10.1029/2007JD009675, 2008.
- 1546
- 1547 Zerefos, C. S., Tourpali, K., Bojkov, R., Balis, D., Rognerund, B., and Isaksen, I.: Solar activity
1548 – total ozone relationships: observations and model studies with heterogeneous chemistry, *J.*
1549 *Geophys. Res.*, *102*, 1561–1569, 1997.
- 1550
- 1551 Ziemke, J. R., A.R. Douglass, L.D. Oman, S.E. Strahan, and B.N. Duncan: Tropospheric ozone
1552 variability in the tropics from ENSO to MJO and shorter timescales, *Atmos. Chem. Phys.*, *15*,
1553 8037–8049, 2015.